THE UNIVERSITY OF CHICAGO

A SEARCH FOR TOP QUARK PAIR PRODUCTION IN THE DILEPTON DECAY MODE

A DISSERTATION SUBMITTED TO
THE FACULTY OF THE DIVISION OF THE PHYSICAL SCIENCES
IN CANDIDACY FOR THE DEGREE OF
DOCTOR OF PHILOSOPHY

DEPARTMENT OF PHYSICS

BY
JAMES C. ROMANO

CHICAGO, ILLINOIS
AUGUST 1995

ACKNOWLEDGEMENTS

This thesis would not have been possible without the hard work of a great many people. I wish to thank all of my collaborators on the CDF experiment and the members of the Fermilab staff, whose efforts make CDF the success that it is.

I would especially like to thank my advisor, Henry Frisch. In the six years I have known him, Henry has always been ready with good suggestions and words of encouragement. Whenever Henry saw me become too deeply mired in the details of this work, he would force me to step back and consider the larger picture. Without Henry's patience and guidance, this thesis could not have been completed. I cannot thank him enough.

Special thanks are owed to Milciades Contreras. Milciades oversaw every detail of this analysis from start to finish, and provided many suggestions for improving it. I also wish to thank the entire Dilepton Working Group, in particular Takeshi Chikamatsu, Jinsong Wang, Lingfeng Song, Qingfang Wang, and G. P. Yeh, all of whom contributed substantially to this analysis.

I wish to thank Sarah Eno, Sacha Kopp, and Jinsong Wang for their help assembling and repairing the trigger electronics, and for sharing the burden of carrying the trigger pager. I would like to thank John Dudas for the masterful modifications he made to the trigger electronics boards. I am grate-

ful to Claudio Campagnari and Marshall Miller for showing me how to use the CDF analysis package, and especially for teaching me the ins and outs of the trigger system. I wish to thank Marty Dippel for keeping the UCCDF cluster running smoothly. I wish to thank my fellow graduate students Sacha Kopp, David Saltzberg, and Jinsong Wang for their help with countless tasks. I would like to thank everyone in the High Energy Physics group at the University of Chicago for making this such a special place to study physics.

I would like to thank my friends who have helped to make my years here as enjoyable as they have been. I am glad for all the time we spent playing softball, volleyball, and golf, throwing darts, brewing beer, grilling burgers, and just generally hanging out.

Finally, I wish to thank my family. My parents and my sister stood behind me every step of the way. This thesis would not have been completed were it not for their love and support.

CONTENTS

LIST OF TABLES

LIST OF ILLUSTRATIONS

ABSTRACT

This thesis presents a search for top quark production through the process $\bar{p}p \rightarrow t\bar{t} + X \rightarrow l^+l^-\nu\bar{\nu}b\bar{b} + X$, where l is either e or μ. Using a sample of 19.3 pb^{-1} of $\bar{p}p$ collisions at $\sqrt{s} = 1.8$ TeV taken at the Tevatron by the Collider Detector at Fermilab during the 1992 – 1993 collider run, we observe 2 events in the signal region, and calculate an expected background of 0.35 ± 0.21 events. The probability for this background to fluctuate to 2 or more events is 6.2%.

Chapter 1

INTRODUCTION

1.1 Why Look for Top?

The known fundamental particles and their interactions, excluding gravity, are described remarkably well by a theory that has come to be known as the Standard Model [1, 2, 3]. Interactions in the Standard Model arise from three gauge symmetries: $SU(3)_{color} \times SU(2)_I \times U(1)_Y$, where I represents weak isospin and Y represents weak hypercharge. The first of these, $SU(3)_{color}$, produces the strong force (QCD), while the latter two, $SU(2)_I \times U(1)_Y$, combine to produce the weak and electromagnetic forces. The three vector fields associated with the $SU(2)_I$ symmetry couple to doublets of left-handed fermions, but not to right-handed fermions. To accommodate this, fermions are grouped into left-handed doublets ($I = 1/2$) and right-handed singlets ($I = 0$). The pairings for the Standard Model quarks and leptons are shown in figure 1.1. There are three generations of quarks and three generations of leptons. The single vector field associated with the $U(1)_Y$ symmetry couples to both left- and right-handed fermions, albeit with different strengths in each of the two

$$\begin{pmatrix} \nu_e \\ e^- \end{pmatrix} \quad \begin{pmatrix} \nu_\mu \\ \mu^- \end{pmatrix} \quad \begin{pmatrix} \nu_\tau \\ \tau^- \end{pmatrix}$$

$$\begin{pmatrix} u \\ d \end{pmatrix} \quad \begin{pmatrix} c \\ s \end{pmatrix} \quad \begin{pmatrix} t \\ b \end{pmatrix}$$

Figure 1.1: The three generations of leptons and quarks in the Standard Model.

Particle	I	I_3	Y	Q
ν_{eL}	1/2	1/2	-1	0
e_L	1/2	$-1/2$	-1	-1
e_R	0	0	-2	-1
u_L	1/2	$-1/2$	1/3	2/3
d_L	1/2	$-1/2$	1/3	$-1/3$
u_R	0	0	4/3	2/3
d_R	0	0	$-2/3$	$-1/3$

Table 1.1: Quantum numbers for the first generation of fermions in the Standard Model. I is the weak isospin, Y is the weak hypercharge, and Q is the electric charge, which may be computed from $Q = I_3 + Y/2$.

cases. Table 1.1 gives these quantum numbers for the first generation of quarks and leptons. The three $SU(2)_I$ vector fields and the single $U(1)_Y$ vector field acquire masses through the Higgs mechanism [4], and mix to form the three massive fields of the weak interaction (W^+, W^-, Z^0), and the massless field (photon) of the electromagnetic interaction. The electric charge of a fermion

can be computed from its weak isospin and weak hypercharge, $Q = I_3 + Y/2$, and these values also appear in Table 1.1.

The discovery of the bottom quark at Fermilab [5] and the subsequent measurements of its properties [6] firmly establish it as the lower component of a quark iso-doublet. The top quark is required to complete the iso-doublet. Furthermore, the top quark is required to fill out the third generation of fermions so that so-called triangle diagrams [3, 7] do not destroy the renormalizability of the Standard Model. These triangle diagrams are a potential problem for the Standard Model, because theories containing both axial and vector couplings of fields to fermions are in general not renormalizable due to anomalies from graphs such as the one in Figure 1.2. These triangle anomalies are proportional to the electric charge of the fermion running around the loop. When the sum over all fermions is performed, the net anomaly is proportional to the sum of the electric charges of all the fermions in the theory. Looking at just the first generation in the Standard Model, we see that this sum is $Q_{tot} = Q_\nu + Q_e + 3Q_u + 3Q_d = 0$, where the factor of three has been inserted because quarks come in three colors. Extending this to the case of three generations, we see that the top quark is needed to keep the theory renormalizable.

1.2 Perspective

This thesis presents a search for the top quark in 19.3 pb^{-1} of data recorded by the CDF detector at the Fermilab Tevatron during 1992 and 1993 [10]. At the time when this analysis was begun, the top quark had not yet been observed. The lower bound on the top quark mass was $m_{top} > 91$ GeV/c^2,

set by the CDF collaboration using 4.1 pb^{-1} of data from an earlier collider run in 1988 – 1989 [8].

During the time between the start of this analysis and the present, there have been several new results published. The D0 collaboration published a lower limit of $m_{top} > 131$ GeV/c^2 from 15 pb^{-1} of data taken during the 1992 – 1993 collider run at Fermilab [9]. From the same collider run, the CDF collaboration published two papers giving evidence supporting the existence of the top quark, with $m_{top} = 174 \pm 17$ GeV/c^2 [10]. The analysis described in this thesis was presented in those publications. A new collider run began in 1994 and is expected to continue through the end of 1995. Both the CDF and D0 collaborations have announced unambiguous observation of the top quark in their increased data samples [11, 12]. It must be noted here that data from the current collider run are not included in this thesis: only the 19.3 pb^{-1} of data recorded in 1992 – 1993 are used. Moreover, the reader should keep in mind that this analysis was performed before the top quark had been observed.

1.3 How to Search for Top

At the Tevatron, the dominant source of top quarks is from $t\bar{t}$ pair production. According to the Standard Model, the top quark decays to a W^+ boson and a b quark, with the charge-conjugate mode for the top antiquark. If the top quark mass is heavier than the sum of the W and b masses, then the W boson will be on its mass shell. Thus, a $t\bar{t}$ pair will decay to two real W bosons and a $b\bar{b}$ quark-antiquark pair. Several different final states are possible, depending on how the W bosons decay. Figure 1.3 diagrams the decay of a $t\bar{t}$ pair, and Table 1.2 shows the branching ratios to each of the final states. The largest branching ratio is for the case when both W bosons decay hadronically.

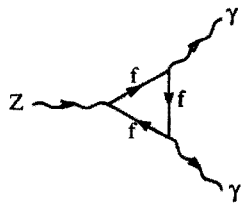

Figure 1.2: A Feynman graph that produces a triangle anomaly.

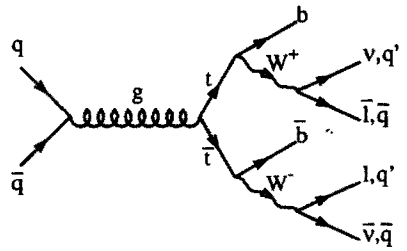

Figure 1.3: Tree-level diagram for $t\bar{t}$ production and decay.

The backgrounds to this mode from QCD multijet production are quite large, making it difficult to observe $t\bar{t}$ production in this channel. The next largest branching ratios occur when one W boson decays leptonically and the other decays to hadrons, leading to a final state with four jets. Frequently referred to as the lepton + jets channel, this mode has a large background from W + multijet production. The background can be greatly reduced by requiring the

Final State	Branching Ratio
$q\bar{q}q\bar{q}b\bar{b}$	36/81
$e\nu q\bar{q}b\bar{b}$	12/81
$\mu\nu q\bar{q}b\bar{b}$	12/81
$\tau\nu q\bar{q}b\bar{b}$	12/81
$e\nu e\nu b\bar{b}$	1/81
$e\nu\mu\nu b\bar{b}$	2/81
$e\nu\tau\nu b\bar{b}$	2/81
$\mu\nu\mu\nu b\bar{b}$	1/81
$\mu\nu\tau\nu b\bar{b}$	2/81
$\tau\nu\tau\nu b\bar{b}$	1/81

Table 1.2: Branching ratios to $t\bar{t}$ final states.

presence of b quarks in the event. This has been done by the CDF and D0 collaborations by looking for the semi-leptonic decay of the b quarks, and by the CDF collaboration by looking for secondary vertices consistent with the b lifetime [11, 12].

As the name suggests, in the dilepton decay channel both W bosons decay leptonically, yielding a final state with two oppositely charged leptons, two neutrinos, and two b quarks. As can be seen from Table 1.2, these decay modes have the smallest branching ratios.

The analysis presented here is a search for $t\bar{t}$ events in the dilepton decay channel. The backgrounds in this channel are lower than in the other channels, compensating for the decreased statistics due to the small branching ratio. Because τ identification is somewhat more difficult than e or μ identification, we consider only the cases where the charged leptons are electrons or muons. Consequently, the final states we are interested in contain two charged leptons (e or μ), two neutrinos, and two b quarks. Because the W boson mass

is approximately 80 GeV/c^2 [42], its decay products will be quite energetic, typically possessing momenta of 40 GeV/c.

The CDF detector is capable of identifying electrons and muons. The b quarks will appear as hadron jets. The neutrinos are not directly observed. Instead, we infer their existence from an imbalance in the transverse components of momentum for the entire event. In this analysis, we look for events with two energetic electrons or muons, two hadron jets from the b quarks, and a momentum imbalance signalling the presence of neutrinos.

There are several $t\bar{t}$ decay modes which may produce final states with two electrons or muons. We are primarily concerned with the case where the leptons come directly from the decay of a W ($W \rightarrow e\nu$, $W \rightarrow \mu\nu$). We may also detect leptons from the decay of a W into a tau, followed by the leptonic decay of the tau, or from the semi-leptonic decay of a b quark, or from the decay $b \rightarrow cX$, followed by the semi-leptonic decay of the c quark. Leptons from these sources tend to be less energetic than those from the direct decay of W bosons, but they may still satisfy the selection criteria. When we calculate the acceptance for this analysis, the contribution from these events is included. For a heavy top, *e.g.* 140 GeV/$c^2 < m_{top} <$ 200 GeV/c^2, approximately 85% of the acceptance is from events where both W's decay to electrons or muons, approximately 11% is from events where one of the leptons comes from the decay of a tau, and the remaining 4% have a lepton from the semi-leptonic decay of a b or c quark.

Chapter 2

DESCRIPTION OF DETECTOR

2.1 Overview

The CDF detector has azimuthal and forward-backward symmetry. We choose coordinates so that the z-axis points along the proton beam direction with $z = 0$ for the nominal interaction point, and the azimuthal angle ϕ is measured from the plane of the Tevatron. We frequently use the variables θ, which is the polar angle from the z-axis, and η, which is the pseudorapidity, defined as $\eta = ln(\cot(\theta/2))$. Figure 2.1 shows a cut-away view of the detector. The portions of the detector relevant for this analysis are the calorimeters, tracking systems, the central muon systems, and the beam-beam counters. Here we will give a brief description of these systems. A more detailed account of the CDF detector may be found in Reference [13].

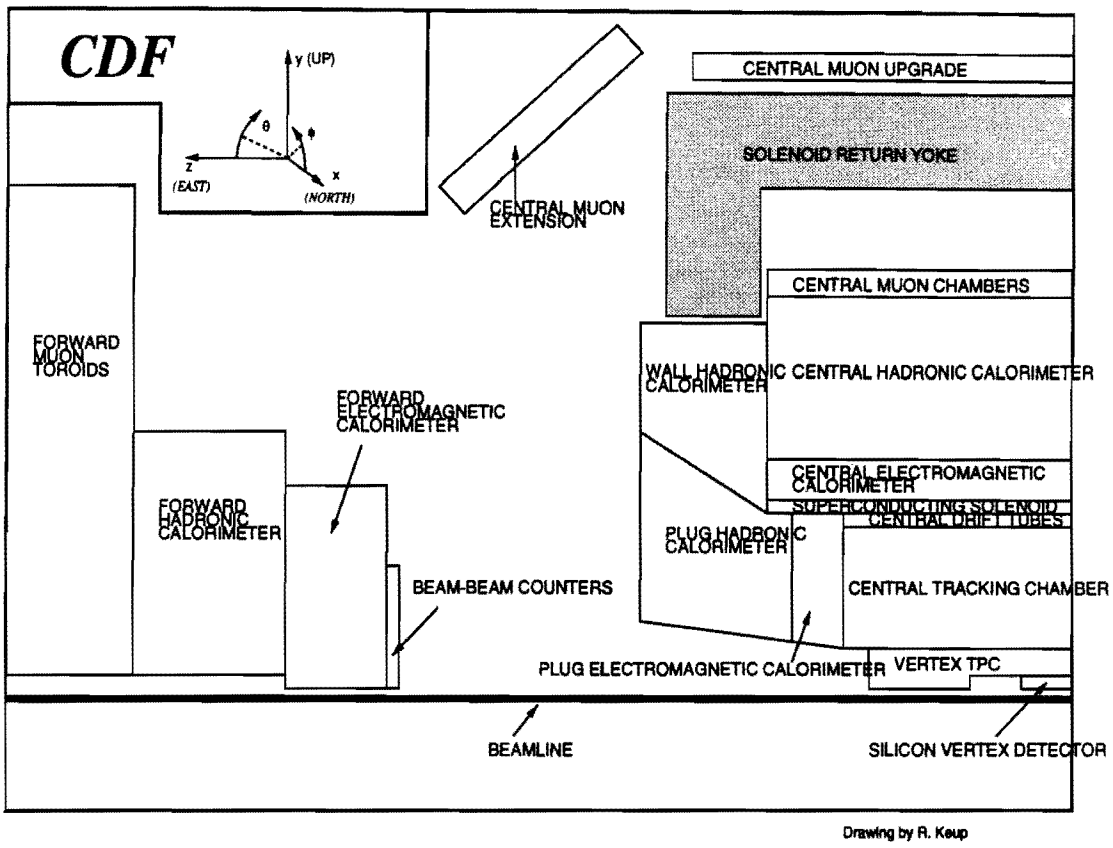

Figure 2.1: A cut-away side view of one half of the CDF detector.

2.2 Tracking Systems

There are three tracking systems which are important for this analysis. In order of increasing radial distance from the beam pipe, these systems are the Silicon Vertex Detector (SVX) [14], the Vertex Drift Chamber (VTX) [15], and the Central Tracking Chamber (CTC) [16].

The SVX is a four layer silicon microstrip detector which surrounds the beam pipe for a total length of 51 cm, with an inner radius of 3.0 cm and an outer radius of 7.9 cm, centered on the nominal interaction point. The

strips are oriented axially and are spaced at 60 μm in the inner three layers, and 55 μm in the outer layer. Each layer provides a position measurement for charged particles with a resolution of 13 μm in the plane transverse to the beam. This allows a measurement of the impact parameter with a resolution of 17 μm for high momentum charged particles. The lifetimes of hadrons containing b quarks are on the order of $\tau \approx 1$ ps, or $c\tau \approx 300$ μm. The SVX is thus capable of identifying secondary vertices from b decay. The efficiency of finding a secondary vertex in a b jet which passes through the SVX ($|\eta| < 1.0$) is approximately 30% [10].

The VTX consists of a series of time projection chambers surrounding the SVX and beamline in the region $|\eta| < 3.25$ and having an outer radius of 22 cm. The VTX finds charged particle tracks in the $r - z$ plane, and is used to measure the z-coordinate of the $\bar{p}p$ interaction with a resolution of 1 mm.

The CTC is a large drift chamber with inner radius 0.3 m, outer radius 1.3 m, and length 3.2 m. There are 84 concentric layers of sense wires. These 84 layers are grouped into 9 superlayers. The wires in 5 of the superlayers run axially, and provide measurements of the position of charged particles in the $r - \phi$ plane. These 5 superlayers are referred to as axial superlayers. The wires in the other 4 superlayers are tilted $\pm 3°$ with respect to the z axis. These 4 tilted superlayers are referred to as stereo superlayers. The spatial resolution of individual CTC hits is approximately 200 μm. Combined with the information from the axial superlayers, hits in the stereo superlayers provide z information for tracks, with a resolution of 6 mm in the z coordinate. The CTC sits inside of a 1.4 T magnetic field produced by a superconducting solenoidal magnet and provides momentum measurements for charged particles. An algorithm is run to fit tracks to the CTC hits. This algorithm is $99.7\% \pm 0.2\%$ efficient at finding tracks for electrons in W events

with $|\eta| < 1.1$ [30]. The resolution of the momentum measurement in units of GeV/c is given by $\sigma_{p_T} \cong 0.002 \times {p_T}^2$, where p_T refers to the transverse components of the momentum in GeV/c, $p_T = P \times \sin\theta$, where θ is the opening angle between the charged particle track and the proton beam direction. Adding the constraint that the track originates from the proton beamline effectively increases the lever arm, and improves the momentum resolution to $\sigma_{p_T} \cong 0.001 \times {p_T}^2$.

2.3 Calorimeters

There are three distinct regions of calorimeter coverage in the CDF detector. These are the central, plug, and forward regions. All three of these regions lie outside the solenoid and tracking systems, and all three contain electromagnetic and hadronic calorimeters arranged in a projective tower geometry, with the towers pointing back to the nominal interaction point. The electromagnetic calorimeters are closer to the interaction point, and use a lead absorber. The hadronic calorimeters lie behind the electromagnetic calorimeters, and use an iron absorber.

The central calorimeter consists of two barrel-shaped halves which meet at the plane $z = 0$. Each half contains 24 wedges, each of which covers 15° in ϕ and $0 < |\eta| < 1.1$. The Central Electromagnetic Calorimeter (CEM) [17] consists of 10 towers in each wedge, so that each tower is approximately 15° in ϕ and 0.1 in η. Each CEM tower contains alternating layers of lead absorber and plastic scintillator, and has a thickness of 18 radiation lengths. Plastic light guides bring the light from the scintillator to two photomultiplier tubes for each CEM tower. The Central Electron Strip (CES) [17] chambers are proportional chambers located within the CEM at a depth of six radiation

lengths, which is near the shower maximum. The CES chambers measure the shower profile in both the transverse ($r - \phi$) and longitudinal (z) views. Each wedge contains two strip chambers which meet at $|\eta| \approx 0.6$.

The Central Hadronic Calorimeter (CHA) and the Wall Hadronic Calorimeter (WHA) [18] towers lie behind the CEM towers, and together they cover the range $|\eta| < 1.3$. Each CHA and WHA tower consists of alternating layers of iron absorber and plastic scintillator, again with light guides to bring the light from the scintillator to photomultiplier tubes. Both the CHA and WHA are 4.5 interaction lengths thick.

The Plug Electromagnetic Calorimeter (PEM) [19], the Plug Hadronic Calorimeter (PHA) [20], the Forward Electromagnetic Calorimeter (FEM) [21], and the Forward Hadronic Calorimeter (FHA) [22] all use alternating layers of gas proportional tubes and lead or iron absorber. Cathode pads of size 5° in ϕ and 0.1 in η collect charge from the tubes. Table 2.1 gives the η coverage, energy resolution, and thickness of the different calorimeter systems.

System	Coverage	Segmentation ($\delta\eta \times \delta\phi$)	Thickness	Energy Resolution (GeV)
CEM	$\|\eta\| < 1.1$	$0.1 \times 15°$	18 X_0, 0.3 Λ_{abs}	$0.135 \times \sqrt{E/(1\text{ GeV})}$
CHA/WHA	$\|\eta\| < 1.3$	$0.1 \times 15°$	4.5 Λ_{abs}	$0.80 \times \sqrt{E/(1\text{ GeV})}$
PEM	$1.1 < \|\eta\| < 2.4$	$0.1 \times 5°$	19 X_0, 1.0 Λ_{abs}	$0.28 \times \sqrt{E/(1\text{ GeV})}$
PHA	$1.3 < \|\eta\| < 2.4$	$0.1 \times 5°$	5.7 Λ_{abs}	$1.30 \times \sqrt{E/(1\text{ GeV})}$
FEM	$2.2 < \|\eta\| < 4.2$	$0.1 \times 5°$	25 X_0, 0.8 Λ_{abs}	$0.25 \times \sqrt{E/(1\text{ GeV})}$
FHA	$2.3 < \|\eta\| < 4.2$	$0.1 \times 5°$	7.7 Λ_{abs}	$1.41 \times \sqrt{E/(1\text{ GeV})}$

Table 2.1: Properties of the CDF calorimeters.

2.4 Muon Chambers

The Central Muon System (CMU) [23] consists of four layers of drift chambers behind each of the 48 central calorimeter wedges. These chambers detect charged particles emerging from the CHA. Behind the CMU chambers is 0.6 m of additional steel shielding. The Central Muon Upgrade System (CMP) [24] consists of four layers of drift chambers outside of this shielding. Both the CMU and CMP extend out to $|\eta| < 0.6$, but neither offers 100% coverage over this range. Of the solid angle with $|\eta| < 0.6$, 53% is covered by both the CMU and CMP chambers, 31% is covered only by CMU chambers, 10% is covered only by CMP chambers, and 6% is not covered by either CMU or CMP chambers.

The Central Muon Extension System (CMX) [25] again consists of four layers of drift chambers and detects charged particles which penetrate through the hadron calorimeters. The segmentation follows that of the central calorimeter wedges; each chamber is 15° in ϕ. The CMX provides muon detection for the range $0.6 < |\eta| < 1.0$. The CMX covers 71% of the solid angle with $0.6 < |\eta| < 1.0$.

2.5 Beam-Beam Counters

Close to the beam pipe and just before the inner faces of the FEM lie the Beam-Beam Counters (BBC) [26]. The BBC system consists of 32 plastic scintillator paddles, 16 each on either side of the interaction region. The BBC system detects charged particles over the range $3.2 < |\eta| < 5.9$. Minimum ionizing particles have typical pulse heights of 300 mV. Discriminators are set to fire at 30 mV. The presence of at least one paddle above threshold on either

side of the interaction region is used to signal the occurrence of a scatter, $\bar{p}p \rightarrow X$.

2.6 Trigger and Data Acquisition

When the Tevatron is operating in colliding mode, there are 6 bunches of protons circulating clockwise (viewed from above) in the ring. These 6 bunches are evenly spaced around the ring, so that there are 60° between neighboring bunches. At the same time, there are 6 bunches of antiprotons circulating counter-clockwise around the ring. A proton bunch and an antiproton bunch pass through each other every 3.5 μs at the center of the CDF detector. Thus, there is a potential $\bar{p}p$ interaction in the CDF detector every 3.5 μs. We employ a three-level trigger system [27, 28] to reduce this 280 kHz rate of potential events to approximately 5 Hz, the maximum rate at which we can write events to tape for storage. The Level 1 and Level 2 trigger decisions are made in hardware by custom-built electronics. The Level 3 trigger decision is made in software by a farm of Silicon Graphics computers running Fortran programs.

The Level 1 and Level 2 trigger decisions must be made more quickly than the detector electronics can be read out. A subset of the full event information is tapped off and carried on dedicated cables directly to the hardware trigger. The hardware trigger implements a coarser calorimeter segmentation than that available offline. In the central region, a trigger cell consists of two adjacent calorimeter towers, so that a trigger cell is 0.2 in η by 15° in ϕ. Analog signals carry the information from the calorimeter to the trigger, and the trigger cell energies are obtained by summing the energies of the two constituent calorimeter towers. The trigger segments each of the 48 CMU muon chambers

into 3 sections, each 5° wide in ϕ. Signals from the muon system to the trigger inform the trigger which of the 5° sections contain hits. This is the full extent of the ϕ information on the muon chamber hits available to the hardware trigger, and there is no η information available. Signals from the Central Tracking Chamber (CTC) supply the Central Fast Tracker (CFT) [29] with the information it needs to perform a two-dimensional $(r-\phi)$ track search for the hardware trigger. Signals from the Beam-Beam Counters (BBC) inform the trigger which of the 32 scintillator paddles are above threshold.

The Level 1 trigger executes each time p and $\overline{p}$ bunches meet in the detector, returning its decision early enough that the detector can be instructed to keep or to clear the event in time for the next p-$\overline{p}$ crossing, so that the Level 1 trigger incurs no deadtime. Because of settling times and cable delays, only about 400 ns of the 3.5 μs between crossings is available for the Level 1 trigger to make its decision. Complicated algorithms therefore cannot be run. The Level 1 trigger only asks whether there is at least one trigger cell with energy above a threshold, if there were hits in a muon chamber, and which of the BBC paddles were above threshold. The track information from the CFT is not available to the Level 1 trigger. At typical instantaneous luminosities of $5 \cdot 10^{30}$ cm^2/s, the Level 1 trigger provides a rejection factor of approximately 100, accepting events at a rate of approximately 2 kHz, compared with the 280 kHz bunch crossing rate.

The Level 2 trigger runs each time the Level 1 trigger accepts an event. The Level 2 trigger takes approximately 20 μs to execute, and the detector is instructed to keep the event it contains and ignore subsequent crossings until the Level 2 trigger has made its decision. For the calorimetry-based triggers (*e.g.,* electron and jet triggers), the Level 2 trigger runs an algorithm to build clusters out of individual trigger cells. These clusters are

then checked against a list of criteria. For the electron triggers, the cluster may be required to have a low ratio of hadronic to electromagnetic energy, and may also be required to have a CFT track pointing towards it in the $r-\phi$ plane. The muon triggers require a CFT track matched (again, in ϕ) to muon chamber hits. The Level 2 trigger provides a rejection factor of approximately 100, accepting events at a rate of approximately 20 Hz.

When the Level 2 trigger accepts an event, the detector electronics are fully read out into computer memory and passed along for examination by the Level 3 trigger. The Level 3 trigger runs the same reconstruction algorithms that are used for offline analyses, but before the run-by-run calibration constants have been entered into the database. The Level 3 trigger is quite flexible, and capable of implementing a large number of sophisticated event selection routines. Some of these routines are designed to accept events for high priority analyses (*e.g.*, the top quark search, W and Z physics), and events which satisfy them are written directly from computer memory to disk. The data sample comprised of these high priority events is referred to as the "express stream." The bulk of the events accepted by the Level 3 trigger do not fall into this category. These events are written from computer memory to tape.

Once the database has been loaded with the appropriate calibration constants, the express stream events are again run through the reconstruction algorithms and then written to tape. Copies of the tapes are distributed to the members of the CDF collaboration. The express stream dataset is contained on 194 8 mm video cassette tapes. Data samples which are small enough to remain on disk are stripped from the tapes of the express stream sample. One of these smaller data samples is the dilepton sample. The dilepton sample is described in Chapter 4 and is the data sample used for this analysis.

Chapter 3

LEPTON AND JET IDENTIFICATION

3.1 Overview

This chapter describes the reconstruction algorithms used to identify electrons, muons, jets, and neutrinos. Both the triggering and offline selection requirements are addressed.

3.2 Electrons

In this analysis, we are concerned with electrons only in the central ($|\eta| < 1.1$) region of the detector. We expect the electron to deposit most of its energy in one or two Central Electromagnetic Calorimeter (CEM) towers, with very little energy deposited in the hadron calorimeter towers behind them. We expect the electron to leave a track in the Central Tracking Chamber (CTC), pointing at the CEM shower.

3.2.1 Electron Fiducial Requirements

To minimize energy mismeasurements, we reject electron candidates where the shower position measured by the Central Electromagnetic Strip (CES) chambers is near a wedge boundary. The shower position is required to be at least 9 cm from the $z = 0$ plane where the two halves of the central calorimeters meet, and at least 3.2 cm from the ϕ boundaries of the wedge. Scintillator coverage extends to within 1.1 cm of the ϕ boundaries, and the CES chambers extend to within 1.7 cm of the ϕ boundaries. Showers are allowed to extend across tower boundaries in η, provided that wedge boundaries are not crossed. There is an algorithm (described below) which attempts to merge the information from towers adjacent in η into a single electron candidate cluster. Recall that there are 10 CEM towers per wedge. We refer to these as Tower 0 through Tower 9, with Tower 0 having the lowest $|\eta|$, and Tower 9 the highest. We require that of the towers in a cluster, the tower with the most energy is not Tower 9. Finally, the region of the CEM with $\eta > 0.8$ and $75° < \phi < 90°$ is not instrumented, as this region provides access for the cryogenics to the solenoid. In terms of CEM towers, this region includes part of Tower 7, all of Tower 8, and all of Tower 9 for that wedge. We refer to this uninstrumented region as the chimney, and exclude it from the allowed fiducial volume.

Figures 3.1 and 3.2 show the distributions of ϕ and η for electrons in the data. The chimney is clearly visible near $0.8 < \eta < 1.0$, $75° < \phi < 90°$. The other obvious hole in this plot, near $255° < \phi < 270°$, $-0.3 < \eta < 0.0$, is due to problems with the CES chambers, and is technically part of the allowed fiducial region. This hole is accounted for when finding the efficiency of the electron identification requirements. In addition to these holes, there are some light areas in the plots. In particular, the region with $345° < \phi < 360°$ and

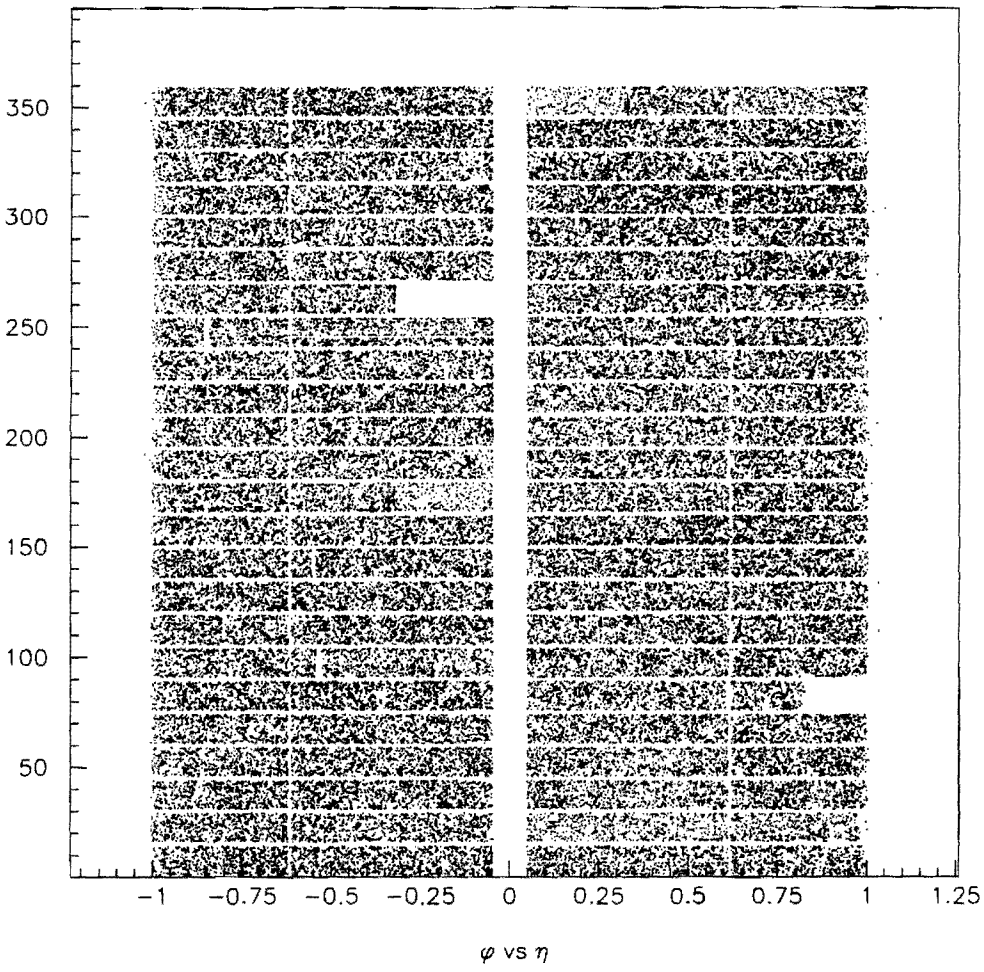

Figure 3.1: A plot of ϕ vs η for central electrons which satisfy the fiducial requirements. This plot was made from the position measured by the CES chambers. The boundary between the two CES modules in each calorimeter wedge and the gaps between wedges are visible.

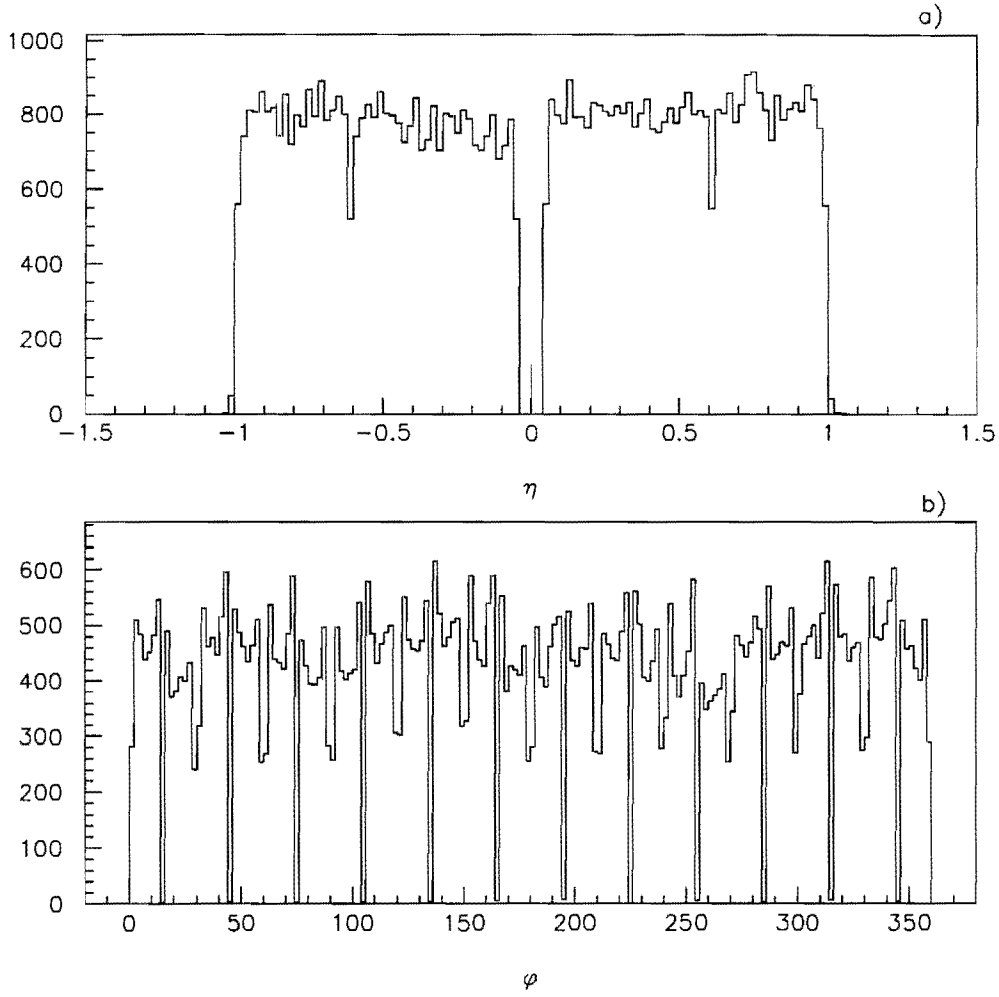

Figure 3.2: The distributions of a) η and b) ϕ for central electrons which satisfy the fiducial requirements. This plot was made from the position measured by the CES chambers.

$0.0 < \eta < 0.3$ and the region with $165° < \phi < 180°$ and $-0.3 < \eta < 0.0$ are less densely populated than are other regions. In both of these cases, problems with the CES chambers cause the lightness in the plots. Again, we account for this inefficiency when computing the efficiencies of the electron identification requirements.

3.2.2 Electron Identification Variables

The first step in reconstructing electrons is to group together individual calorimeter towers to form a single electron candidate. The clustering algorithm begins by choosing a single CEM tower as a potential seed tower. The seed tower must have at least 3 GeV of E_T deposited in it, where E_T, the transverse energy, is defined by $E_T = E \times \sin\theta$, and θ is the opening angle between the electron direction and the proton beam direction. The seed tower will usually be the highest energy tower in the cluster. The CEM seed tower and the Central Hadronic Calorimeter (CHA) or Wall Hadronic Calorimeter (WHA) tower behind it are included in the cluster. The two neighbors in η to the CEM seed tower are added to the cluster, unless the seed tower was Tower 0 or Tower 9, in which case only one neighbor is added. The CHA (or WHA) tower that is grouped into the same trigger cell as the hadronic tower behind the seed tower is also added to the cluster. The ratio of the total hadronic energy in the cluster to the total electromagnetic energy in the cluster is computed. If this ratio is greater than 12.5%, the cluster is rejected. If the ratio is less than that value, the cluster is kept as a potential electron candidate.

The transverse energy, E_T^{em}, of the electron candidate is found by summing the E_T from the three (or two) CEM towers in the cluster. Another ratio of hadronic energy to electromagnetic energy is computed, this time using

the CHA (or WHA) towers behind all the CEM towers in the cluster. We use the symbol E^{had}/E^{em} for this ratio.

We look for CTC tracks which point at the calorimeter cluster. Matches are made between the extrapolated track position and the shower position as measured by the CES. These strip-track matches are made in both the $r-\phi$ view, Δx, and z view, Δz. The ratio of the calorimeter energy to the track momentum, $E_T^{em}/{p_T}^{track}$, is computed. Bremsstrahlung radiation may cause this ratio to be significantly different from unity. The CTC track measures the momentum of the electron after it has radiated. The radiated photons will normally enter the same CEM tower as the electron, so the CEM energy measurement corresponds to the electron's energy before it has radiated.

We fit the CES shower profile in the z view to the expected shower profile for electrons. The quantity χ^2_{strip} gives the χ^2 of the fit between the observed shower shape and the nominal shower shape determined from test beam electrons. We also compare the sharing of energy between CEM towers to the expected lateral sharing for electrons, and define another χ^2-like variable, L_{shr} to measure this agreement. More specifically,

$$L_{shr} = 0.14 \cdot \sum_i \frac{E_i^{obs} - E_i^{exp}}{\sqrt{0.14^2 \cdot E + \sigma^2_{E_i^{exp}}}}$$

where the sum is over the CEM towers adjacent to the seed tower, E_i^{obs} is the energy observed in the tower, E_i^{exp} is the energy expected in the tower, determined from test beam electrons, $\sigma_{E_i^{exp}}$ is the uncertainty in the expected energy, and $0.14 \cdot \sqrt{E}$ is the resolution of the energy measurement. Figure 3.3 shows the distributions for the electron identification variables.

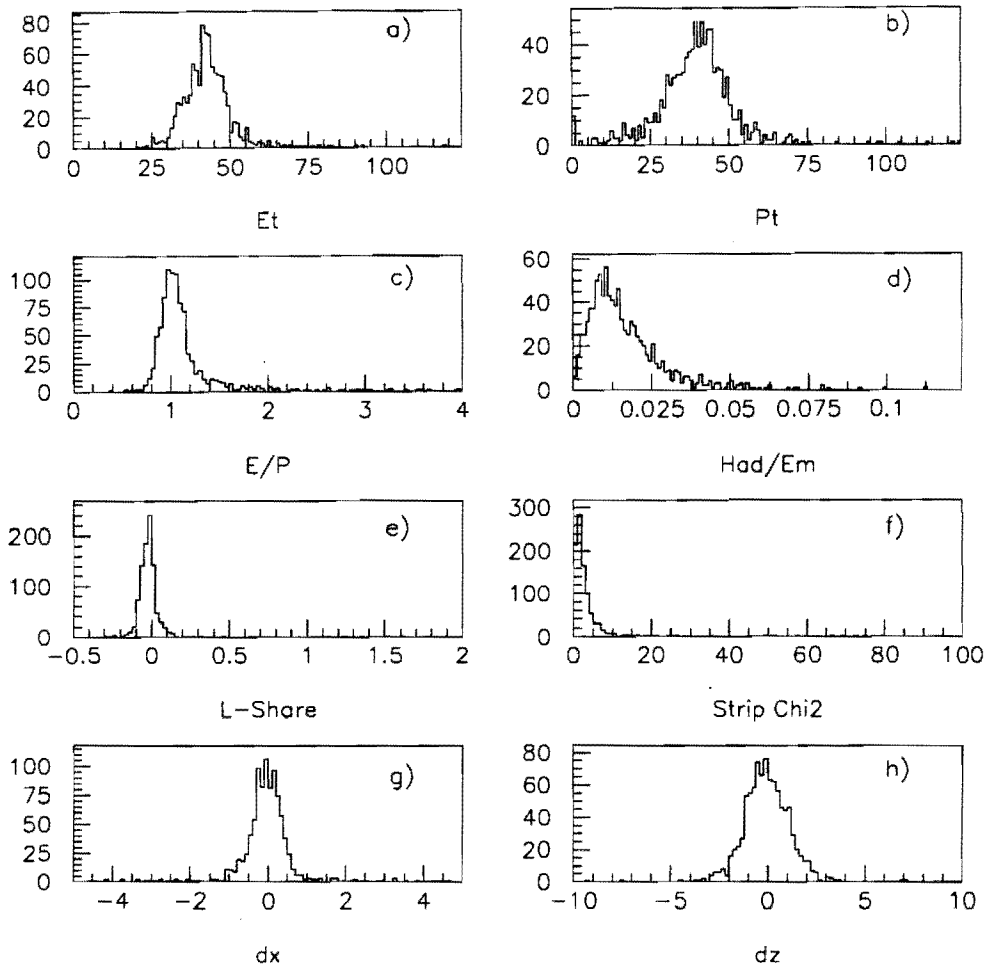

Figure 3.3: Distributions of the variables used for electron identification. The distributions shown are for isolated electrons in Z events. a) The E_T^{em} spectrum, measured by the CEM calorimeter, in GeV; b) the p_T spectrum, measured in the Central Tracking Chamber, in GeV/c; c) the energy/momentum ratio, $E_T^{em}/{p_T}^{track}$; d) the ratio of hadronic to electromagnetic calorimeter energies, E^{had}/E^{em}; e) the lateral sharing variable L_{shr}; f) the shower profile variable χ^2_{strip}; g) the CTC track to CES shower position match in the $r-\phi$ view, Δx, measured in cm; h) the CTC track to CES shower position match in the z coordinate, Δz, measured in cm.

3.2.3 Electron Triggers

The Level 1 central electron trigger requires a hit in at least one of the Beam Beam Counter (BBC) paddles on each side of the interaction region. Further, it requires that at least one CEM trigger cell contains $E_T > 6$ GeV. Averaged over the entire data sample, this trigger is estimated to be 99.2±0.1% efficient [30] for electrons with $E_T > 10$ GeV in an allowed fiducial region, using events that pass the Level 1 and Level 2 muon triggers.

The Level 2 central electron trigger makes use of both calorimetry and tracking information. CEM trigger cells with at $E_T > 9$ GeV become trigger cluster seeds. Neighboring CEM trigger cells with $E_T > 7$ GeV are added to the trigger cluster. The hadronic trigger cells behind the CEM trigger cells are also added to the cluster. The Level 2 central electron trigger requires that the ratio of hadronic-to-electromagnetic energy of the trigger cluster be less than 12.5%. Additionally, the trigger requires that there is a track with $p_T > 9.2$ GeV/c found by the Central Fast Tracker (CFT). The efficiency of this trigger, averaged over the entire data sample, is measured to be 91.5±0.3% for electrons which satisfy the fiducial requirements from W decay, by using W events that satisfy independent triggers [30]. The CFT track requirement contributes most of the inefficiency.

The Level 3 central electron trigger requires a electron candidate cluster with $E_T^{em} > 18$ GeV, a CTC track with $p_T > 13$ GeV/c, $L_{shr} < .2$, $\chi^2_{strip} < 10$, $|\Delta x| < 3$ cm, and $|\Delta z| < 10$ cm. The average efficiency of this trigger is measured to be 98.2 ± 0.1% efficient [30] for W electrons in an allowed fiducial region by using W events which come in on independent triggers. Events with an electron satisfying the requirements of this Level 3 trigger are written to disk and become part of the express stream. The

combined trigger efficiency for central electrons from W decay is estimated to be $89.2 \pm 0.3\%$ [30].

3.3 Muons

We expect muons to produce tracks in the CTC. Muons with $p_T >$ 20 GeV/c are expected to deposit energies of approximately 400 MeV and 2 GeV in the electromagnetic and hadronic calorimeters, respectively. All other charged particles are expected to be absorbed by the central calorimeters, and to deposit all of their energy therein. If, after exiting the calorimeters, the muon strikes a muon chamber in either the Central Muon System (CMU), the Central Muon Upgrade System (CMP), or the Central Muon Extension System (CMX), we expect to see hits in each of the four layers of drift tubes in that muon chamber. These hits should lie on a straight line. The signature for a muon is thus a track in the CTC, small but non-zero energy deposited in the calorimeter towers which the track is projected to hit, and hits in the muon chambers towards which the track points if there is muon chamber coverage there. Muon candidates backed by hits in a muon chamber are referred to as CMUO muon candidates. Muon candidates without muon chamber hits are referred to as CMIO muon candidates. For CMIO muon candidates, cuts are placed on the extrapolated track position in the calorimeters to ensure that the charged particle passed through an active region of the calorimeters.

3.3.1 Muon Fiducial Requirements

For both CMUO and CMIO muon candidates, we impose quality cuts on the CTC track. Specifically, we require that the track has hits in at least 6

superlayers. Of these 6 superlayers, at least 3 must be axial superlayers, and at least 2 must be stereo superlayers. This requirement rejects tracks at high $|\eta|$ which exit through the end wall of the CTC before crossing the minimum number of superlayers.

We require CMUO muon candidates to have hits in either the CMU, CMP, or CMX muon chambers. For CMIO candidates, we ask that the track points at a well-instrumented region of the calorimeters. We require that the track strikes the calorimeter at $|\eta| < 1.2$. The boundary region between the CEM and PEM calorimeters, defined as $1.06 < |\eta| < 1.12$, is also excluded. In the central region, we extrapolate the track to the inner radius of the CEM. We require the extrapolated track position is at least 9 cm from the $z = 0$ boundary where the two halves of the central calorimeters meet, and also that the track position is at least 2.5 cm from the nearest ϕ boundary. Finally, we require that the the CTC track does not strike the chimney. Figures 3.4 and 3.5 show the ϕ and η distributions for muons with CMU and CMP muon chamber hits. Figures 3.6 and 3.7 show the ϕ and η distributions for muons with CMX muon chamber hits. Note that for all these figures, ϕ and η are computed from the muon chamber hits. The muon chambers utilize a charge-division technique to measure the z coordinate of the hits. The CMX chambers do not measure the z coordinate very accurately, with the result that it is sometimes found to be outside of the muon chamber boundary. This explains why there are values of $|\eta|$ greater than 1.2 in Figures 3.6 and 3.7.

3.3.2 Muon Identification Variables

The muon momentum is taken to be the p_T of the track. A better measurement of the muon p_T is obtained if the track is refit with the constraint

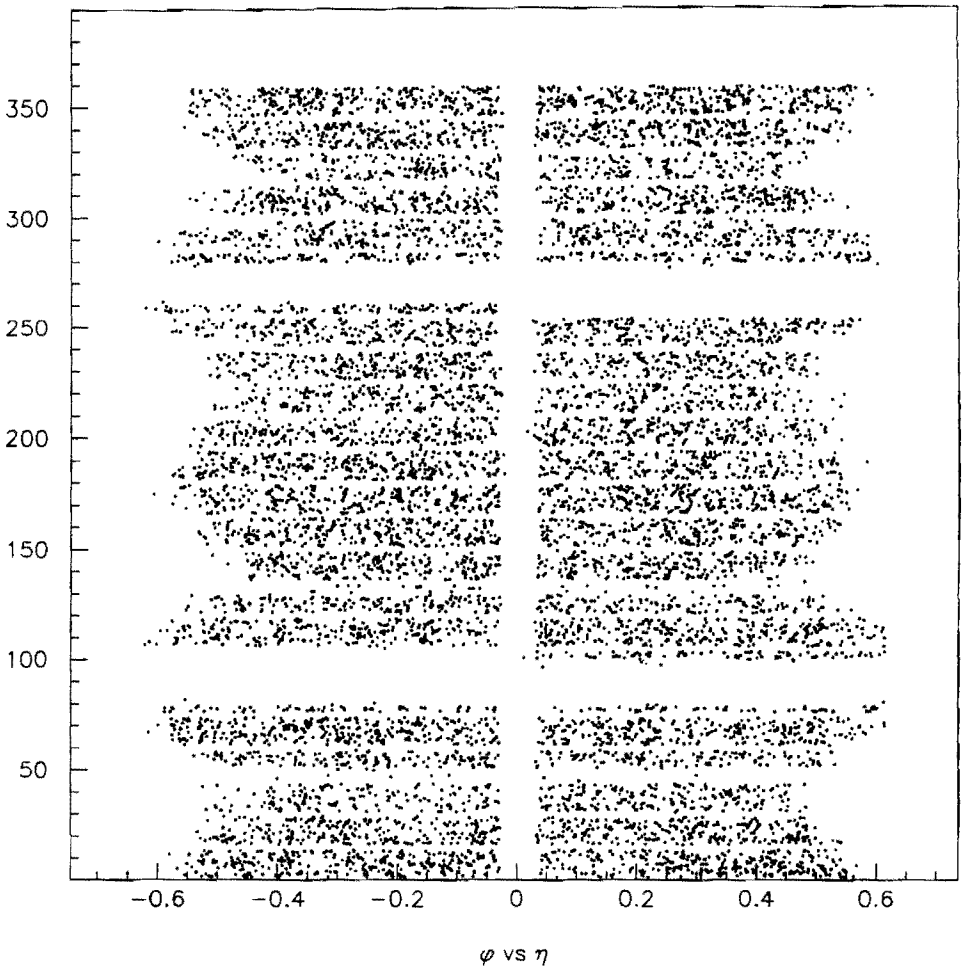

Figure 3.4: A plot of ϕ vs η for muons in the data which have hits in both the CMU and CMP muon chambers. ϕ and η are calculated from the position of the CMU muon chamber hits.

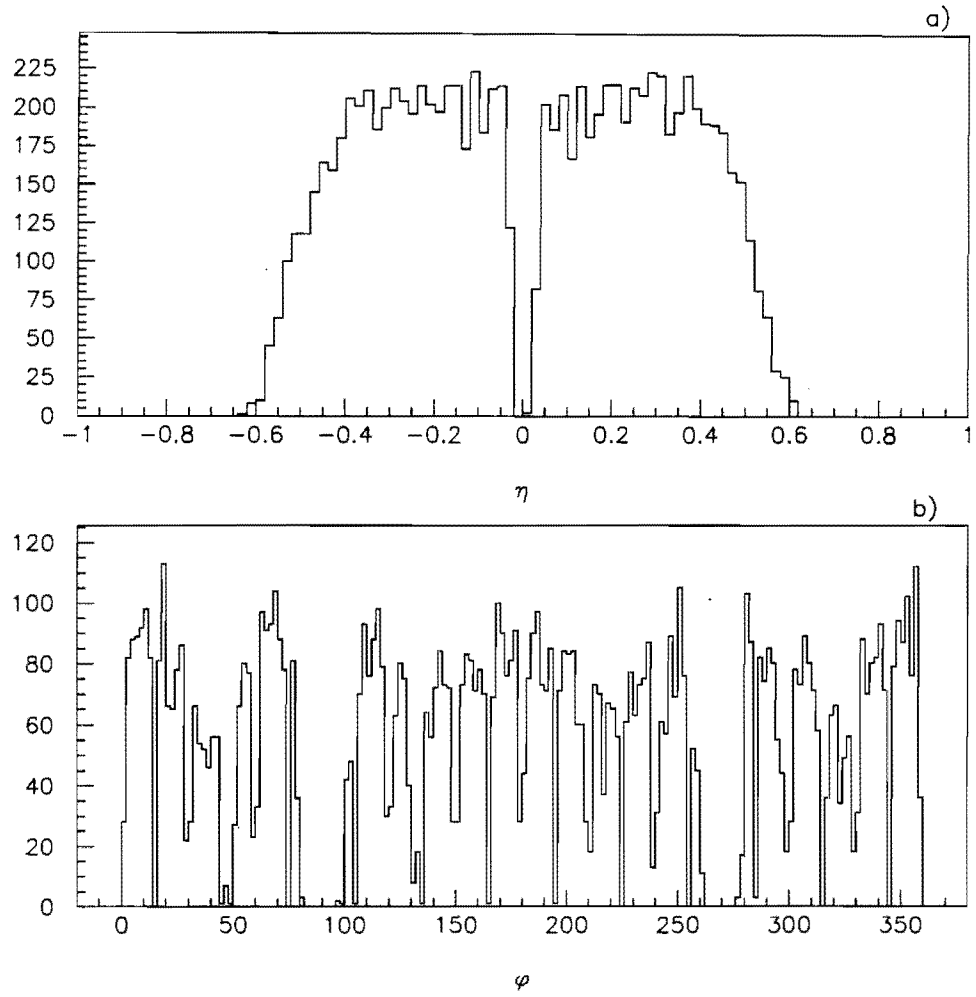

Figure 3.5: The distributions of a) η and b) ϕ for muons in the data which have hits in both the CMU and CMP muon chambers. ϕ and η are calculated from the position of the CMU muon chamber hits.

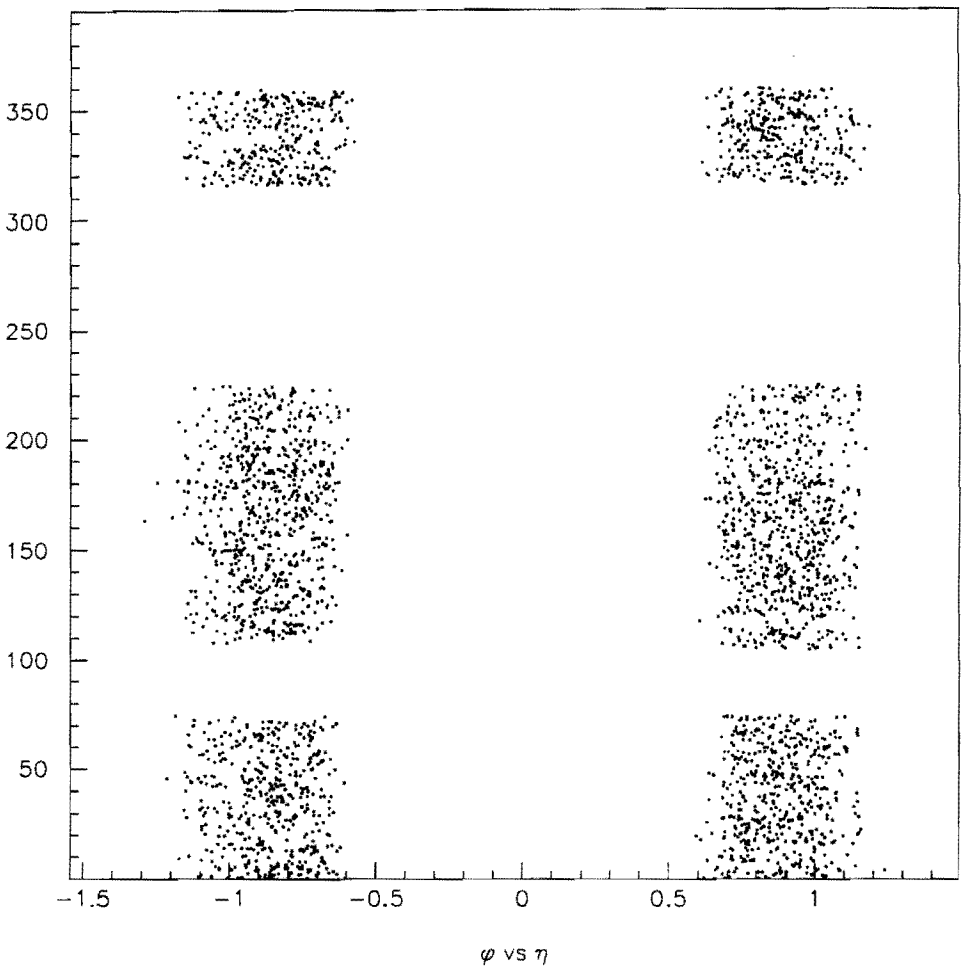

Figure 3.6: A plot of ϕ vs η for muons in the data which have hits in the CMX muon chambers. ϕ and η are calculated from the position of the CMX muon chamber hits.

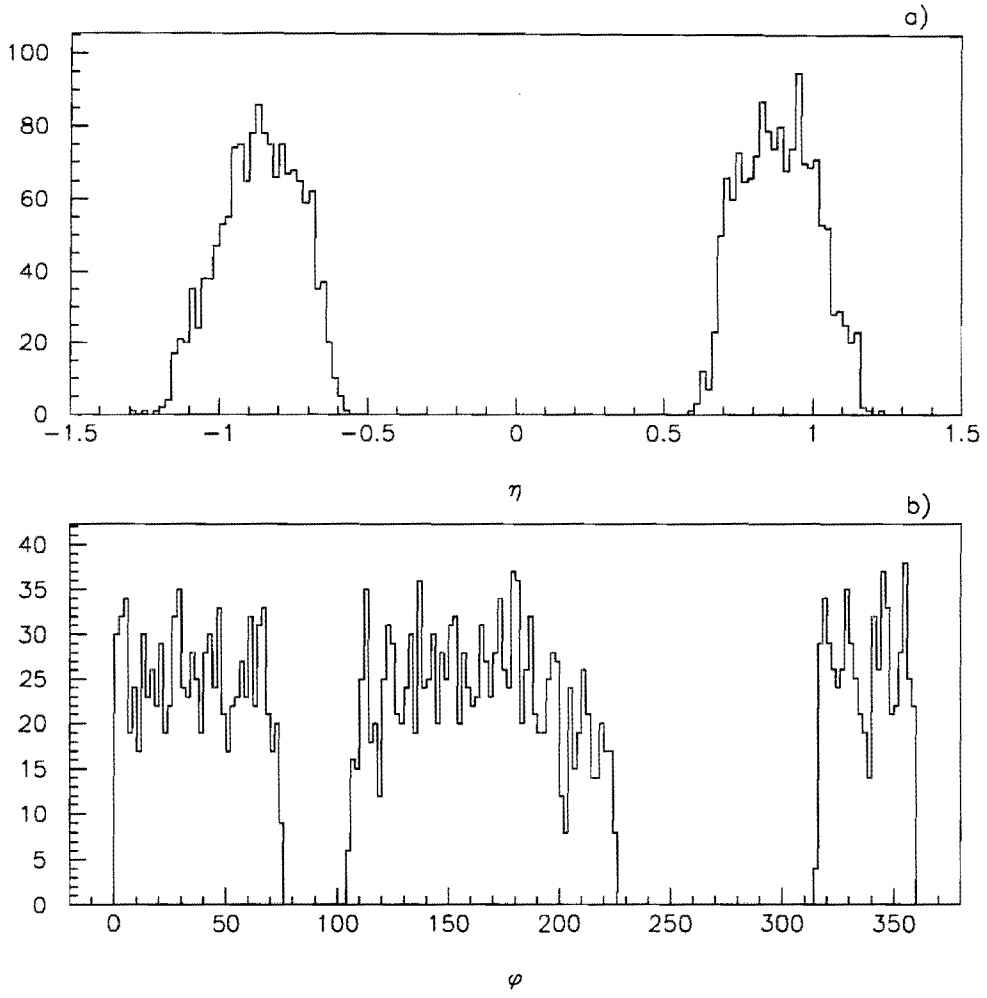

Figure 3.7: The distributions of a) η and b) ϕ for muons in the data which have hits in the CMX muon chambers. ϕ and η are calculated from the position of the CMX muon chamber hits.

that it passes through the beam line. The impact parameter, d_0, of the unconstrained track is measured. This is the distance of closest approach of the track to the proton beam line. Also, the distance in the z direction from the point of closest approach to the nearest vertex found by the Vertex Tracking Chamber (VTX), $\Delta z^{vrt-trk}$, is measured. Figure 3.8 shows the distributions of the quantities for muons in Z events.

We propagate the track through the calorimeters and to the muon chambers. A sum of the energies in all the calorimeter towers through which the track is projected to pass is made. Separate sums are made for electromagnetic energy, E^{em}, and hadronic energy, E^{had}. For CMUO muons, the particle trajectory is extrapolated out to the muon chambers, and the distance in the $r-\phi$ view between the extrapolated track position and the position of the hits in the muon chamber, is measured. This distance is used as a criterion when determining the quality of the match between the track and muon chamber hits. The distributions for these quantities are shown in Figure 3.8 for muons in Z events.

3.3.3 Muon Triggers

The Level 1 muon trigger requires hits in the a Central Muon System (CMU) muon chamber. As described in Chapter 2, the hardware trigger divides each CMU muon chamber into 3 5° sections. If the 5° section containing the hits is backed by a Central Muon Upgrade System (CMP) chamber, then hits are also required in that CMP chamber. There are 72 5° sections on each side of the plane $z = 0$, and 51 of these 72 are backed by CMP chambers. Using a sample of $Z \rightarrow \mu\mu$ events, this trigger is measured to be $95.9 \pm 1.5\%$ efficient [31].

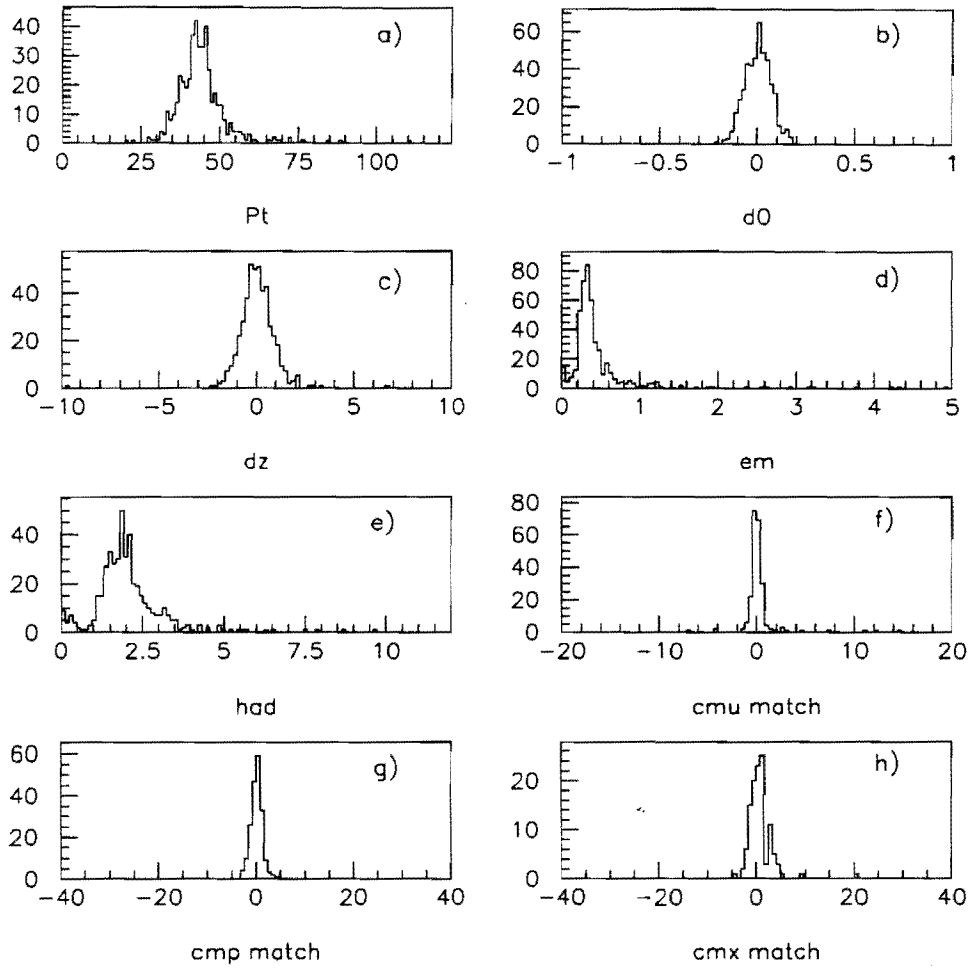

Figure 3.8: Distributions of the variables used for muon identification. The distributions are shown for isolated muons in Z events. a) The p_T spectrum of the beam-constrained tracks, in GeV/c; b) the impact parameter of the unconstrained tracks, d_0, in cm; c) the difference in cm between the origin of the track and the nearest vertex found by the Vertex Tracking Chamber (VTX), $\Delta z^{vrt-trk}$; d) the energy deposited by the muon in the electromagnetic calorimeter, E^{em}; e) the energy deposited by the muon in the hadronic calorimeter, E^{had}; f) the distance in cm between the extrapolated track position and the CMU chamber hits in the $r-\phi$ view; g) the distance in cm between the extrapolated track position and the CMP chamber hits in the $r-\phi$ view; h) the distance in cm between the extrapolated track position and the CMX chamber hits in the $r-\phi$ view.

The Level 2 muon trigger requires a 9.2 GeV/c CFT track in addition to the muon chamber hits required by the Level 1 trigger. The efficiency of the Level 2 muon trigger is determined by the Central Fast Tracker (CFT) tracking efficiency. Using a sample of $W \rightarrow e\nu$ events, this efficiency is measured to be $92.3 \pm 0.9\%$ efficient [31]. As a check, the Level 2 muon trigger efficiency has also been measured from a sample of $Z \rightarrow \mu\mu$ events and is found to be $92.1 \pm 2.0\%$ [31], in good agreement with the number from $W \rightarrow e\nu$ events.

The Level 3 muon trigger requires a track with $p_T > 18$ GeV/c, $E^{had} < 6$ GeV, and a 5 cm or better match between the track and the CMU chamber hits. This trigger is measured to be $98.6 \pm 1.1\%$ efficient [31] using a $Z \rightarrow \mu\mu$ sample. Events which contain a muon satisfying the requirements of this Level 3 trigger are written to disk and become part of the express stream. The combined trigger efficiency for muons is the product of these numbers, or $87.3 \pm 1.9\%$ [31].

3.4 Jets

Because of color confinement, we do not see individual quarks or gluons produced in the $\bar{p}p$ collisions. Rather, these partons hadronize and appear as sprays of particles in the detector. These sprays are usually referred to as "jets," and are spread out over several calorimeter towers. As an estimate of the original parton energy, we sum together the energies in the calorimeter towers within $R < 0.4$ of the largest-energy calorimeter tower in the jet, where $R = \sqrt{(\Delta\eta)^2 + (\Delta\phi)^2}$ and ϕ is in radians. Of course, this only accounts for the fraction of the jet energy which was deposited in an active region of the calorimetry and inside the cone described by $R < 0.4$. In order to get a more accurate estimate of the initial parton energy, we scale up the observed energy

by a correction factor, typically about 1.4. This correction factor depends on the observed jet energy and on its location in the calorimeters, and is found by balancing jet energies in QCD multijet events [32]. Aside from the uncertainty in the energy scale calibration, the uncertainty in the jet energy measurement, in GeV, is approximately $100\%\sqrt{E}$. In addition, we assign a 10% uncertainty to the jet energy scale [10].

If the initial parton is a b quark, the ratio of observed jet energy to parton energy will be different than if the initial parton were a light quark or gluon, and correction factors for b quark jets have also been calculated [10]. The energy resolution for b quark jets corrected in this manner is $20\% \times E$. Figure 3.9 shows E_T spectra of jets in the data, before corrections, after the generic jet corrections, and after the b quark corrections. These b quark corrections are not used in the event selection requirements of this analysis. However, when giving the characteristics of events which satisfy the event selection criteria, jets may be corrected as if they were b quark jets.

3.5 Neutrinos

We do not directly observe neutrinos in the detector. Instead, we rely on momentum conservation and look for an imbalance in the components of momentum transverse to the beam. The vector $\not\!\!E_T$ is defined to be the opposite of the vector sum of the transverse components of the momenta of all the observed particles in an event. If this vector sum is significantly different from zero, we attribute the imbalance to the presence of one or more neutrinos. We use beam-constrained muon momenta when computing the vector sum. Also, jets with uncorrected transverse energy, ${E_T}^{raw}$, above 10 GeV and $|\eta| < 2.4$ are corrected using the generic jet correction, and these corrected energies are

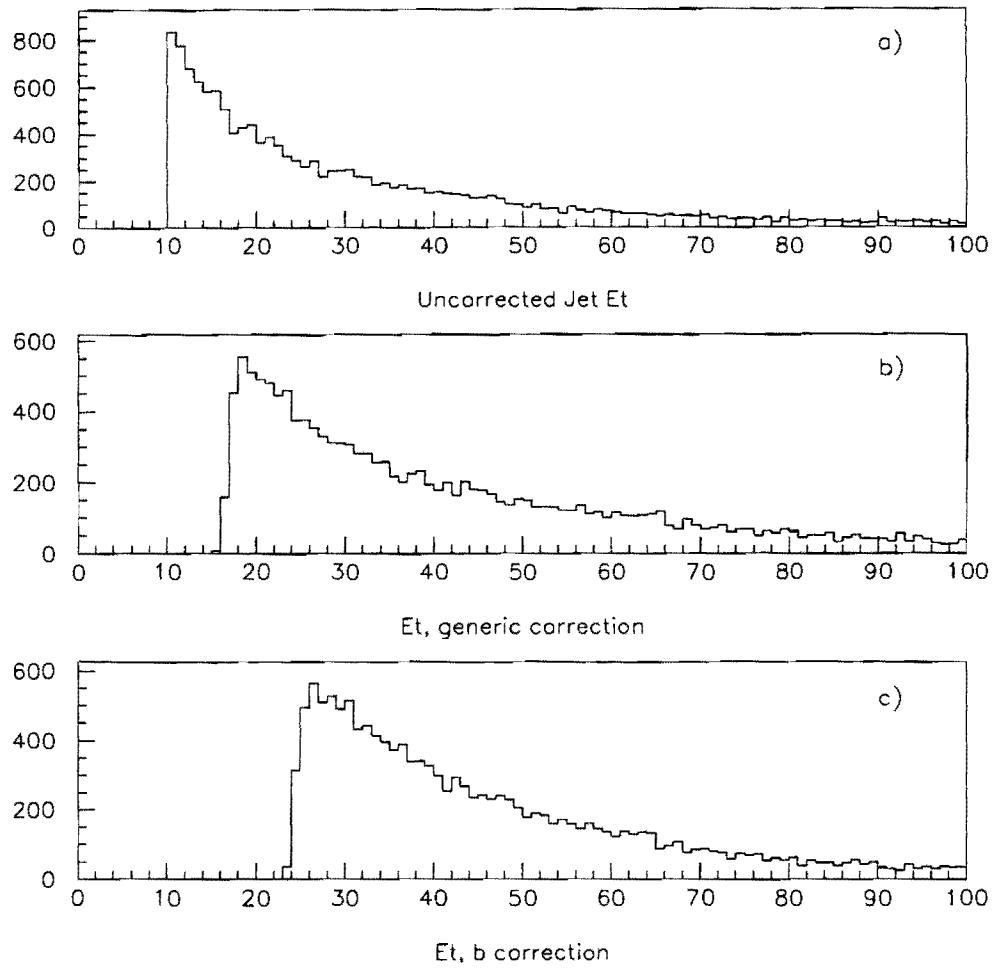

Figure 3.9: Transverse energy, in GeV, of jets with $E_T{}^{raw} > 10$ GeV and $|\eta| < 2.4$ in the data. a) uncorrected energy, $E_T{}^{raw}$; b) corrected energy treating the jet as a generic (light quark or gluon) jet; c) corrected energy treating the jet as a b quark jet.

used when calculating the $\not\!\!E_T$ vector. The uncertainty in the $\not\!\!E_T$ vector is given by the uncertainties in the momenta of all the observed particles in the event.

Chapter 4

EVENT SELECTION

4.1 The Data Sample

The final states we are searching for contain two leptons (e or μ), large $\not\!\!E_T$, and at least two jets. The first step in looking for these events is to create a data sample in which to search for them. The cuts on this sample must be loose enough to keep the events we are looking for, but tight enough that the number of events in the sample is not too unwieldy.

To make the most basic data sample used in this analysis, known as the dilepton sample, we sift through the approximately 1.7 million express stream events looking for events which contain two lepton (e or μ) candidates. Events must have one lepton passing a primary set of requirements and another passing a secondary set of requirements in order to be included in the dilepton sample. Table 4.1 lists the lepton identification cuts used for the dilepton sample. The p_T cut on the leptons is 15 GeV/c, and the lepton identification requirements on the secondary lepton are quite loose. In addition to the cuts listed in Table 4.1, muon candidates with hits in the Central Muon

System (CMU) muon chambers but without hits in the Central Muon Upgrade System (CMP) muon chambers are required to satisfy a position matching cut between the hits in the CMU muon chamber and the extrapolated track position. The cut value is 10 cm in the $r - \phi$ view. No position matching cuts are placed on hits in the CMP muon chambers or Central Muon Extension System (CMX) muon chambers. Events where both leptons are muons must have muon chamber hits left by at least one of the muons in order to be included in the dilepton sample. It should be noted that events where one of the two leptons is an electron in the plug calorimeter are also accepted into the dilepton sample. These electrons in the plug calorimeter are not used in this analysis, and their selection criteria are not described here. Out of the events written to the express stream, 87046 events make it into the dilepton sample. This is the sample that serves as the starting point for this analysis.

Primary e	Secondary e
$E_T^{em} > 15$ GeV $p_T{}^{track} > 10$ GeV/c $E^{had}/E^{em} < 0.055 + 0.045 \times E_T^{em}/100$ $\chi^2_{strip} < 15$	$E_T^{em} > 15$ GeV $p_T{}^{track} > 10$ GeV/c
Primary μ	Secondary μ
$p_T{}^{track} > 15$ GeV/c $E^{em} < 2$ GeV $E^{had} < 6$ GeV	$p_T{}^{track} > 15$ GeV/c

Table 4.1: Selection criteria for the dilepton data sample.

4.2 Geometrical and Kinematical Acceptance

As mentioned in Chapter 1, there are sources of electrons and muons in $t\bar{t}$ other than direct W decay. These additional sources include leptonic τ decay, and semi-leptonic decay of b and c quarks. Figure 4.1 shows the p_T spectra for leptons from each of these sources in $t\bar{t}$ Monte Carlo events, generated with the ISAJET Monte Carlo program [39] at a top mass, m_{top}, of 160 GeV/c^2 [47]. The lepton p_T spectra depend on the top mass, especially for those leptons from b and c decay. In this analysis, we look for events with two leptons (e or μ), each of which must have at least 20 GeV/c of p_T. This p_T cut is motivated by the desire to have good efficiency for the electrons and muons from W decay, while reducing the expected backgrounds from, for instance, $\bar{p}p \rightarrow b\bar{b}$ events. The p_T cut at 20 GeV/c rejects many of the leptons from non-W sources in the $t\bar{t}$ Monte Carlo, but keeps most of the leptons from the direct decay of the W (see Figure 4.1), and is necessary to keep the backgrounds from $b\bar{b}$ events small. Table 4.2 shows the fraction of $t\bar{t}$ Monte Carlo events which have two or more 20 GeV/c leptons (e or μ), for several values of m_{top}. The numbers for p_T cuts at 15 and 25 GeV/c are also shown. Note that the fraction of $t\bar{t}$ final states where both W's decay leptonically (to e or to μ) is $4/81 = 0.049$. The fiducial requirements for electrons and muons have been discussed in Chapter 3. To find the efficiency of the fiducial cuts, we take $t\bar{t}$ Monte Carlo events generated with the ISAJET program, and simulate the response of the CDF detector with the QFL detector simulation program [33]. Figure 4.2a shows the $\eta - \phi$ distribution of 20 GeV/c electrons and muons in $t\bar{t}$ Monte Carlo events, generated using $m_{top} = 160$ GeV/c^2. Figure 4.2b shows

m_{top}(GeV/c^2)	A_{p_T} $p_T > 15$ GeV/c	A_{p_T} $p_T > 20$ GeV/c	A_{p_T} $p_T > 25$ GeV/c
100	$.051 \pm .001$	$.038 \pm .001$	$.027 \pm .001$
120	$.068 \pm .001$	$.046 \pm .001$	$.031 \pm .001$
140	$.086 \pm .001$	$.057 \pm .001$	$.039 \pm .001$
160	$.102 \pm .001$	$.068 \pm .001$	$.046 \pm .001$
180	$.118 \pm .001$	$.081 \pm .001$	$.056 \pm .001$
200	$.133 \pm .001$	$.092 \pm .001$	$.064 \pm .001$

Table 4.2: Fraction of $t\bar{t}$ Monte Carlo events with two leptons (e or μ) with p_T above a threshold.

the distribution after the fiducial cuts have been applied. Table 4.3 shows the combined efficiency of the p_T and fiducial cuts. The numbers in this table are the fraction of $t\bar{t}$ Monte Carlo events which have two or more leptons (e or μ) passing the p_T and fiducial requirements after the QFL detector simulation program has been run. Losses to due inefficiencies of the lepton reconstruction algorithms have been included in this table.

m_{top}(GeV/c^2)	$A_{geom \cdot p_T}$
100	$.016 \pm .001$
120	$.021 \pm .001$
140	$.026 \pm .001$
160	$.032 \pm .001$
180	$.037 \pm .001$
200	$.043 \pm .001$

Table 4.3: Fraction of $t\bar{t}$ Monte Carlo events with two 20 GeV/c electrons or muons in the fiducial region accepted by this analysis, versus m_{top}.

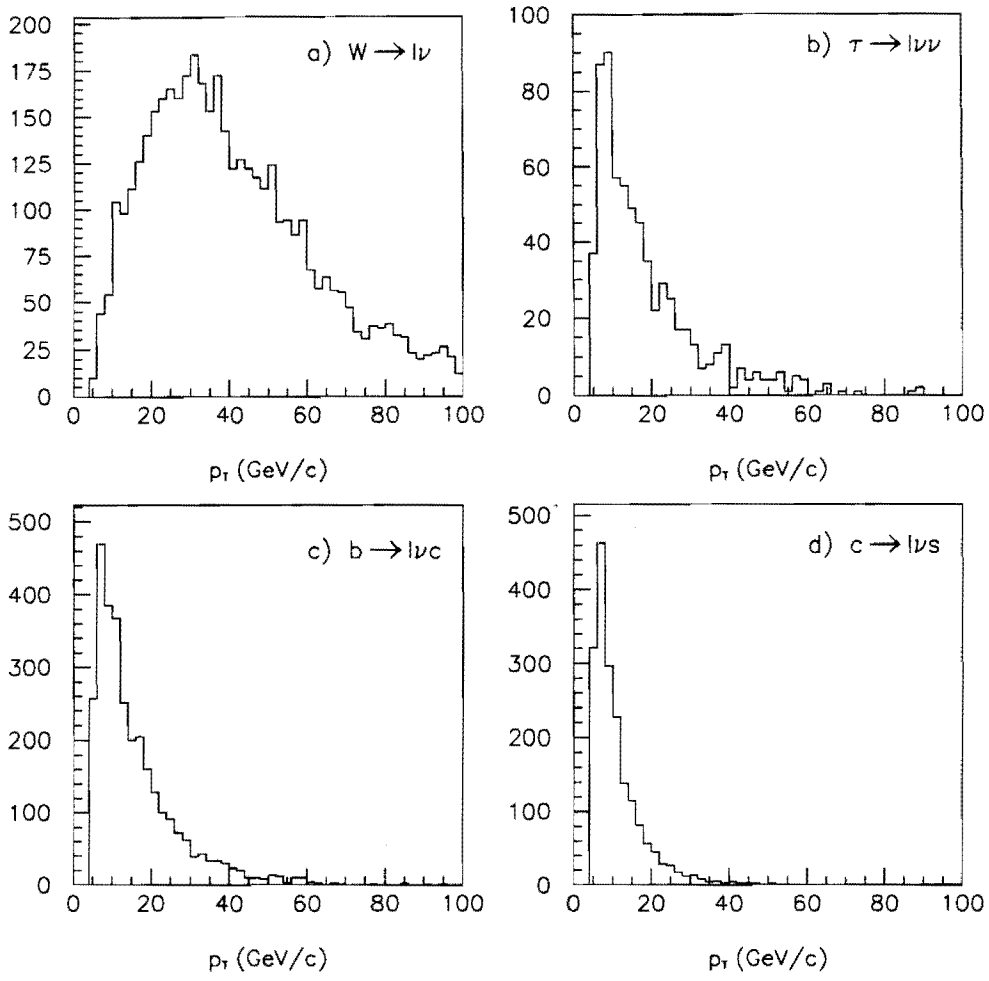

Figure 4.1: The p_T spectra for electrons and muons in $t\bar{t}$ Monte Carlo events, generated with $m_{top} = 160$ GeV/c^2: a) leptons from W decay; b) leptons from τ decay; c) leptons from semi-leptonic b decay; d) leptons from semi-leptonic c decay. All four plots are from the same sample of 10,000 events.

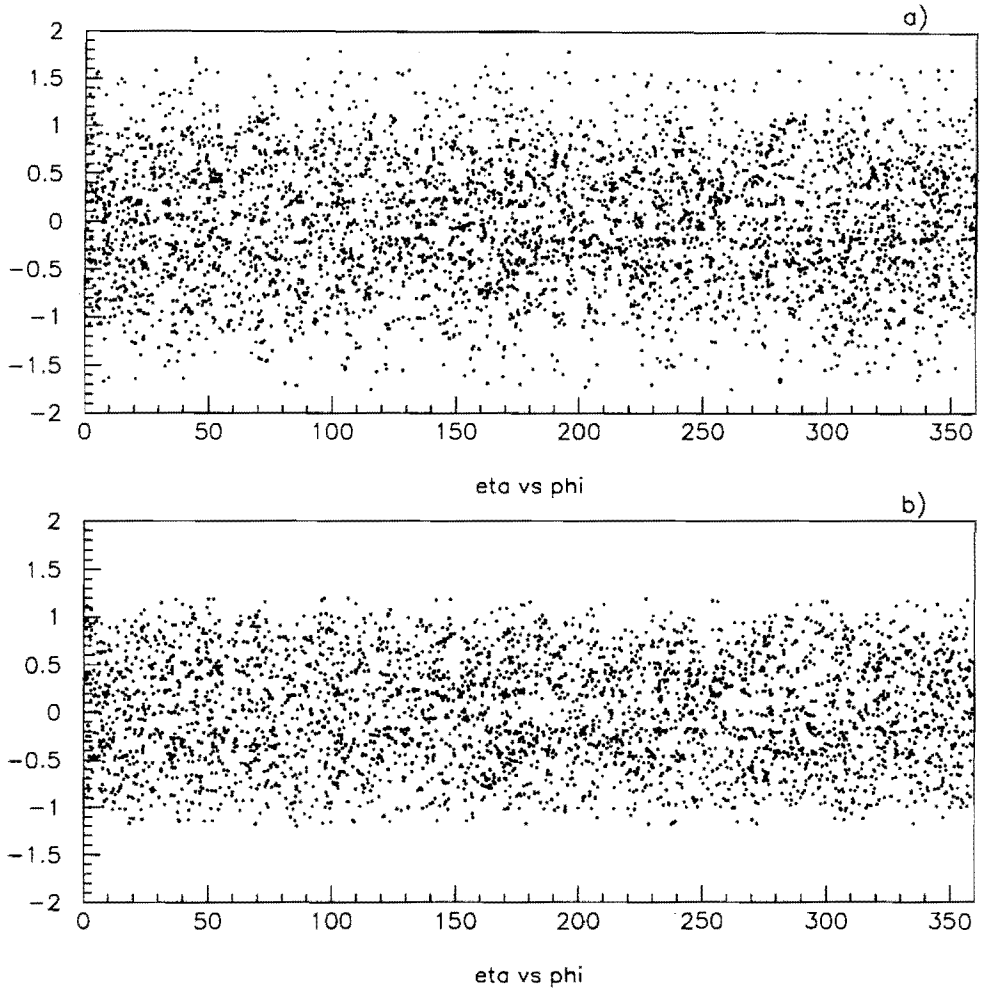

Figure 4.2: The plot of η *vs* ϕ for 20 GeV/c electrons and muons in $t\bar{t}$ Monte Carlo events, generated with $m_{top} = 160$ GeV/c^2: a) before fiducial cuts; b) after fiducial cuts.

4.3 Lepton Identification Requirements

The lepton identification variables are described in Chapter 3. Here we list the cuts we make on these quantities in order to select dilepton events. For electrons, we define two sets of lepton identification cuts, which we label "tight" and "loose." For muons, we use the same set of cuts for both CMUO and CMIO muons.

For the ee mode, we require one electron candidate passing the tight electron identification cuts, and another electron candidate passing the loose electron identification cuts. For the $e\mu$ mode, the electron candidate must pass the tight electron identification cuts, and the muon candidate must pass the muon identification cuts. For the $\mu\mu$ mode, both muon candidates must pass the muon identification criteria, and at least one of the muon candidates must have hits in both the Central Muon System (CMU) chambers and Central Muon Upgrade System (CMP) chambers. This requirement is made to ensure that at least one of the two muon candidates in the event is capable of satisfying the Level 1 and Level 2 trigger requirements.

4.3.1 Electron Cuts

Table 4.4 lists the lepton identification requirements for tight and loose electrons. In both cases, we require at least 20 GeV of E_T deposited in the Central Electromagnetic Calorimeter (CEM) and a track with p_T above 10 GeV/c. We run an algorithm [40] to identify electrons from photon conversions ($\gamma \rightarrow e^+e^-$), and reject the potential conversion electrons. Further cuts include a cut on the ratio of hadronic to electromagnetic energy deposition in the calorimeters, E^{had}/E^{em}; a cut on the ratio of the transverse energy deposited in the CEM to the track transverse momentum, $E_T^{em}/{p_T}^{track}$; matching

between the extrapolated track position and the centroid of the electromagnetic shower in the CEM as measured by the Central Strip Chambers (CES) in both the $r-\phi$ and z directions, Δx and Δz, respectively; a cut on the shape of the shower profile, again as measured by the CES, χ^2_{strip}; and a cut on the sharing of energy between neighboring CEM towers, L_{shr}. These quantities are described in more detail in Chapter 3.

Tight Central Electron Cuts	Loose Central Electron Cuts
$E_T^{em} > 20$ GeV	$E_T^{em} > 20$ GeV
${p_T}^{track} > 10$ GeV/c	${p_T}^{track} > 10$ GeV/c
$E^{had}/E^{em} < 0.05$	$E^{had}/E^{em} < 0.055 + 0.045 \times E_T^{em}/100$
$E_T^{em}/{p_T}^{track} < 2$	$E_T^{em}/{p_T}^{track} < 4$
$\Delta x < 1.5$ cm	$\Delta x < 1.5$ cm
$\Delta z < 3.0$ cm	$\Delta z < 3.0$ cm
$L_{shr} < 0.2$	$L_{shr} < 0.2$
$\chi^2_{strip} < 15$	

Table 4.4: Selection criteria for tight and loose electrons.

4.3.2 Muon Cuts

Muons will generally leave only about 400 MeV of energy in the electromagnetic calorimeter and about 2 GeV of energy in the hadronic calorimeter, whereas other charged particles will deposit all of their energy in the calorimeters. We require that the electromagnetic, E^{em}, and hadronic, E^{had}, energy depositions are consistent with the expectations for muons. Cosmic ray muons passing through the CDF detector may satisfy these calorimetry requirements. In order to reject cosmic ray muons, we require that the track has an impact parameter, d_0, of less than 3 mm. Additionally, we require that the distance in z, $\Delta z^{vrt-trk}$, between this point of closest approach to the pro-

ton beam line and the nearest vertex found in the Vertex Tracking Chamber (VTX) is less than 5 cm. These cuts are made before the beam constraint is applied to the track. As a further safeguard against cosmic rays, we reject muon candidates which are back-to-back within 0.1 in η and 1.5° in ϕ of another muon candidate.

For CMUO muon candidates, we place cuts on the distance between the position of the hits in the muon chamber and the direction of the track. For CMIO muon candidates, we impose more stringent fiducial requirements (see Chapter 3) to guarantee that they strike an active region of the calorimetry. The matching cuts for CMUO muons are cuts on the distance in the $r - \phi$ plane between the position of the hits in the muon chamber and the position of the track extrapolated out to the muon chamber. The cut values are 10 cm for hits in the CMU chambers, 20 cm for hits in the CMP chambers, and 20 cm for hits in the CMX chambers. These matching requirements are "or"ed together, so that a CMUO muon candidate with both CMU and CMP hits present need only pass the matching cuts to one of the two in order to satisfy the muon identification requirements as a whole. Table 4.6 shows that these matching requirements are nearly 100% efficient.

A more detailed discussion of the muon identification variables is given in Chapter 3. Table 4.5 lists the muon identification requirements.

4.3.3 Efficiencies

The efficiencies of the electron and muon identification cuts listed above are affected by the presence of other particles near the lepton. Because of this, the lepton identification efficiencies depend on the source of the leptons. Leptons from b decay, for instance, will be accompanied by nearby hadronic

Muon Identification Cuts
$p_T^{track} > 20$ GeV/c
$E^{em} < 2$ GeV
$E^{had} < 6$ GeV
$E^{em} + E^{had} > 0.1$ GeV
$d_0 < 3$ mm
$\Delta z^{vrt-trk} < 5$ cm
position match if CMUO muon
calorimeter fiducial cut if CMIO muon

Table 4.5: Selection criteria for muons.

Muon System Present	Efficiency of Matching Cuts	
	Data	Monte Carlo
CMU	1.000 ± 0.029	1.000 ± 0.022
CMP	1.000 ± 0.056	1.000 ± 0.024
CMU and CMP	1.000 ± 0.011	1.000 ± 0.007
CMX	0.992 ± 0.019	1.000 ± 0.010

Table 4.6: Efficiency[41] of the muon position matching cuts for muons from $Z \rightarrow \mu^+\mu^-$ decays in data and in ISAJET+QFL Monte Carlo.

particles which may cause the lepton to fail some of the identification cuts, whereas leptons from Z decay will generally be more isolated and therefore more likely to pass the identification cuts. To estimate the lepton identification efficiencies in $t\bar{t}$ events, we use the ISAJET program to generate $t\bar{t}$ events, and then simulate the detector response with the QFL [33] detector simulation program. As a check that QFL models the detector response correctly, we use ISAJET and QFL to generate and simulate $Z \rightarrow ee$ and $Z \rightarrow \mu\mu$ events, and compare the lepton identification efficiencies in the Z Monte Carlo to those found from Z events in the data. Table 4.7 gives the efficiencies of the electron identification cuts for $Z \rightarrow ee$ events in the data and in the ISAJET+QFL

Monte Carlo. These efficiencies are for electrons with $E_T^{em} > 20$ GeV which pass the fiducial requirements. Table 4.8 gives the efficiencies of the muon identification cuts for $Z \rightarrow \mu\mu$ events in the data and in the ISAJET+QFL Monte Carlo. These efficiencies are for muons with ${p_T}^{track} > 20$ GeV/c and which pass the fiducial requirements.

	$\epsilon^{tight\ e}$		$\epsilon^{loose\ e}$	
Cut	Data	Monte Carlo	Data	Monte Carlo
${p_T}^{track}$	$.977 \pm .006$	$.988 \pm .003$	$.977 \pm .006$	$.988 \pm .003$
E^{had}/E^{em}	$.971 \pm .007$	$.851 \pm .009$	$.995 \pm .004$	$.946 \pm .006$
$E_T^{em}/{p_T}^{track}$	$.936 \pm .009$	$.957 \pm .005$	$.976 \pm .006$	$.985 \pm .003$
Δx	$.921 \pm .010$	$.965 \pm .005$	$.921 \pm .010$	$.965 \pm .005$
Δz	$.964 \pm .007$	$.992 \pm .003$	$.964 \pm .007$	$.992 \pm .003$
L_{shr}	$.980 \pm .006$	$.980 \pm .004$	$.980 \pm .006$	$.980 \pm .004$
not conversion	$.957 \pm .008$	$.977 \pm .004$	$.957 \pm .008$	$.977 \pm .004$
χ^2_{strip}	$.964 \pm .007$	$.990 \pm .003$		
all cuts	$.807 \pm .014$	$.765 \pm .011$	$.856 \pm .012$	$.869 \pm .009$

Table 4.7: Efficiency of electron identification requirements from $Z \rightarrow e^+e^-$ decays in data and in ISAJET+QFL Monte Carlo.

The QFL efficiencies in Z events agree fairly well with the efficiencies measured from data, but it will be noted that the agreement is not perfect. When we use ISAJET+QFL $t\bar{t}$ Monte Carlo events to extract the lepton identification efficiencies in $t\bar{t}$ events, we scale the Monte Carlo efficiencies by the ratio of efficiencies in Z events in data and Monte Carlo. These scale factors are 1.055 and 0.985 for tight and loose electrons, respectively. For CMUO muons, the correction factor is 0.956, and for CMIO muons, the correction factor is 0.934. For CMUO muons which are capable of satisfying the Level 1 and Level 2 triggers, the correction factor is 0.953. Table 4.9 lists the efficien-

$\epsilon^{trigger\ CMUO}$		
Cut	Data	Monte Carlo
E^{em}	0.969 ± 0.020	0.996 ± 0.009
E^{had}	0.982 ± 0.018	0.988 ± 0.011
$E^{em} + E^{had}$	1.000 ± 0.011	1.000 ± 0.007
d_0	0.994 ± 0.014	1.000 ± 0.007
$\Delta z^{vrt-trk}$	0.994 ± 0.014	1.000 ± 0.007
position match	1.000 ± 0.011	1.000 ± 0.007
all cuts	0.939 ± 0.025	0.985 ± 0.012
ϵ^{CMUO}		
Cut	Data	Monte Carlo
E^{em}	0.968 ± 0.012	0.995 ± 0.005
E^{had}	0.984 ± 0.009	0.984 ± 0.007
$E^{em} + E^{had}$	0.992 ± 0.008	1.000 ± 0.003
d_0	0.997 ± 0.006	1.000 ± 0.003
$\Delta z^{vrt-trk}$	0.992 ± 0.008	1.000 ± 0.003
position match	0.997 ± 0.006	1.000 ± 0.003
all cuts	0.936 ± 0.015	0.979 ± 0.007
ϵ^{CMIO}		
Cut	Data	Monte Carlo
E^{em}	0.955 ± 0.035	0.984 ± 0.016
E^{had}	0.955 ± 0.035	0.989 ± 0.014
$E^{em} + E^{had}$	1.000 ± 0.021	1.000 ± 0.010
d_0	1.000 ± 0.021	1.000 ± 0.010
$\Delta z^{vrt-trk}$	1.000 ± 0.021	1.000 ± 0.010
all cuts	0.909 ± 0.042	0.973 ± 0.018

Table 4.8: Efficiency[41] of muon identification requirements from $Z \rightarrow \mu^+\mu^-$ decays in data and in ISAJET+QFL Monte Carlo. The efficiency of the muon identification cuts for muons which are capable of firing the Level 1 and Level 2 muon triggers (*i.e.*, muons with hits in both the CMU and CMP muon chambers) are given by $\epsilon^{trigger\ CMUO}$. The efficiency of the muon identification cuts for all muons which leave hits in a muon chamber is given by ϵ^{CMUO}, and the efficiency of the muon identification cuts for muons which do not leave hits in a muon chamber is given by ϵ^{CMIO}.

cies of the lepton identification cuts (after corrections) for leptons from various sources in $t\bar{t}$ Monte Carlo events with $m_{top} = 160$ GeV/c^2. Table 4.10 gives the fraction of all $t\bar{t}$ events which have two leptons passing the p_T, fiducial, and lepton identification requirements of this analysis.

	Source of Electron or Muon			
	W	τ	b	c
$\epsilon^{tight\ e}$	0.73 ± 0.01	0.74 ± 0.03	0.09 ± 0.01	0.04 ± 0.02
$\epsilon^{loose\ e}$	0.81 ± 0.01	0.80 ± 0.03	0.13 ± 0.01	0.07 ± 0.02
$\epsilon^{trigger\ CMUO}$	0.91 ± 0.01	0.85 ± 0.03	0.20 ± 0.02	0.03 ± 0.02
ϵ^{CMUO}	0.91 ± 0.01	0.86 ± 0.02	0.19 ± 0.01	0.03 ± 0.01
ϵ^{CMIO}	0.90 ± 0.01	0.84 ± 0.05	0.19 ± 0.03	0.10 ± 0.04

Table 4.9: Efficiency of lepton identification requirements for leptons in $t\bar{t}$ Monte Carlo events, generated with $m_{top} = 160$ GeV/c^2. These numbers have been scaled by the ratio of efficiencies measured in data and in Monte Carlo Z events.

m_{top}(GeV/c^2)	ee	$e\mu$	$\mu\mu$	Total
100	$.0022 \pm .0001$	$.0056 \pm .0002$	$.0024 \pm .0002$	$.0102 \pm .0003$
120	$.0023 \pm .0002$	$.0060 \pm .0002$	$.0031 \pm .0002$	$.0115 \pm .0003$
140	$.0027 \pm .0002$	$.0071 \pm .0003$	$.0032 \pm .0002$	$.0129 \pm .0004$
160	$.0029 \pm .0002$	$.0072 \pm .0003$	$.0038 \pm .0002$	$.0139 \pm .0004$
180	$.0029 \pm .0002$	$.0074 \pm .0003$	$.0040 \pm .0002$	$.0143 \pm .0004$
200	$.0032 \pm .0002$	$.0073 \pm .0003$	$.0038 \pm .0002$	$.0144 \pm .0004$

Table 4.10: Fraction of $t\bar{t}$ Monte Carlo events with two 20 GeV/c leptons passing the lepton identification requirements and fiducial requirements.

4.4 Isolation Cuts

The lepton identification cuts are designed to distinguish electrons and muons from hadrons. Because hadrons are so readily produced in the $\overline{p}p$ collisions we are studying, in the data there will be hadrons that satisfy the lepton identification requirements. We can reduce the number of hadrons faking leptons by asking that the lepton candidates are well-separated from other particles in the event. The quantity which measures how well-separated a particle is from its neighbors is is referred to as isolation. Because hadrons are generally produced in jets, they are usually not very isolated. We expect the directions of the leptons from W decay in $t\bar{t}$ events to be only weakly correlated with each other and with the directions of the b jets, and so these leptons will usually have a much higher degree of isolation than do hadrons.

We employ two types of isolation cuts in this analysis. Firstly, all CMIO muons are required to be isolated in the calorimeter. That is, the sum of the E_T in the calorimeter towers near the calorimeter towers through which the muon passed must be less than 5 GeV. The calorimeter towers which contain the muon are not included in the sum, but all other towers within $\Delta R < 0.4$, where $\Delta R = \sqrt{(\Delta\eta)^2 + (\Delta\phi)^2}$, are included. Secondly, we require that at least one of the two charged leptons in the event passes a tracking isolation cut. The tracking isolation cut is a cut on the sum of the transverse momenta (p_T) of all tracks within a cone of radius $\Delta R < 0.25$ of the lepton track. The lepton track itself is not included in the sum, and we require that the sum be less than 3 GeV/c. Table 4.11 gives the efficiencies of the isolation cuts for events which pass the p_T, fiducial, and lepton identification cuts, for several values of m_{top}.

m_{top}(GeV/c^2)	ee	$e\mu$	$\mu\mu$
100	0.991 ± 0.012	0.962 ± 0.010	0.970 ± 0.014
120	0.991 ± 0.012	0.953 ± 0.010	0.937 ± 0.016
140	0.984 ± 0.012	0.952 ± 0.009	0.946 ± 0.015
160	0.986 ± 0.011	0.942 ± 0.010	0.917 ± 0.016
180	1.000 ± 0.007	0.950 ± 0.009	0.932 ± 0.014
200	0.990 ± 0.009	0.925 ± 0.011	0.912 ± 0.016

Table 4.11: Fraction of $t\bar{t}$ Monte Carlo events passing the p_T, fiducial, and lepton identification requirements which pass the isolation cuts[41].

4.5 Event Topology Cuts

4.5.1 Z Rejection

In the ee and $\mu\mu$ channels, we expect a large number of events from Z decay. Figure 4.3 shows the invariant mass distributions for dielectron and dimuon data events passing the p_T, fiducial, lepton identification, and isolation cuts listed above, along with the dilepton invariant mass in $t\bar{t}$ Monte Carlo for $m_{top} = 160$ GeV/c^2. For this analysis, we reject ee and $\mu\mu$ events where the invariant mass of the leptons is between 75 and 105 GeV/c^2. Table 4.12 gives the efficiency of the Z removal cut for $t\bar{t}$ events which pass the p_T, fiducial, lepton identification and isolation cuts.

4.5.2 $\not\!\!E_T$ Cuts

We expect the signal events to contain two neutrinos, leading to an observed imbalance of transverse energy in the detector. To cut down on the number of background events we expect, we require events to have $\not\!\!E_T > 25$ GeV, where $\not\!\!E_T$ is the magnitude of the $\not\!\!E_T$ vector. As mentioned in

m_{top}(GeV/c^2)	ee	$\mu\mu$
100	0.761 ± 0.033	0.754 ± 0.030
120	0.786 ± 0.031	0.748 ± 0.026
140	0.750 ± 0.030	0.764 ± 0.026
160	0.726 ± 0.030	0.757 ± 0.024
180	0.747 ± 0.029	0.755 ± 0.023
200	0.734 ± 0.028	0.802 ± 0.022

Table 4.12: Fraction of $t\bar{t}$ Monte Carlo events passing the p_T, fiducial, lepton identification, and isolation requirements which survive the Z removal cuts.

Chapter 3, beam-constrained momenta are used for the muon p_T, and jets with ${E_T}^{raw} > 10$ GeV and $|\eta| < 2.4$ are corrected using the generic jet corrections when computing the $\not\!\!E_T$ vector. The b quark jet corrections are not used for calculating $\not\!\!E_T$.

There are still potential backgrounds which contain two leptons and large $\not\!\!E_T$, including $Z \rightarrow \tau\tau$ where both τ's decay leptonically, and production of e^+e^- and $\mu^+\mu^-$ pairs in association with jets. In the first of these cases, the leptonic decay of each tau produces two neutrinos, which may result in a large value of $\not\!\!E_T$. The $\not\!\!E_T$ vector in these events frequently points near the direction (in ϕ) of one of the τ's, and consequently near the direction (in ϕ) of the e or μ into which the τ decayed.

Jet energy mismeasurement in events containing e^+e^- or $\mu^+\mu^-$ pairs may result in large values of $\not\!\!E_T$. When this happens, it is usually the case that the jet energy is underestimated, and the $\not\!\!E_T$ vector will point into or near the mismeasured jet.

In order to reduce the backgrounds from the processes described above, we ask that the angle in ϕ between the $\not\!\!E_T$ vector and the nearest lepton or jet, $\Delta\phi_{min}$, is greater than 20° for events where the magnitude of

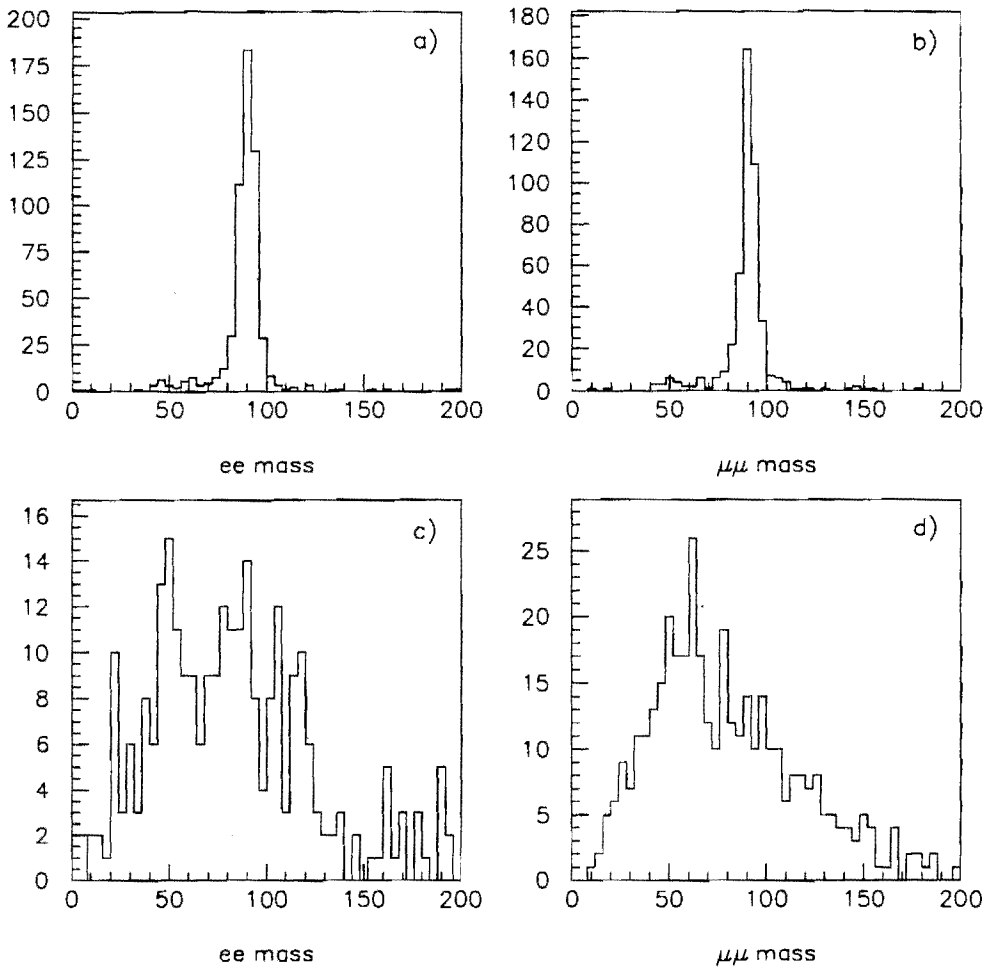

Figure 4.3: The lepton-lepton invariant mass spectra: a) dielectron events in the data; b) dimuon events in the data; c) dielectron events in $t\bar{t}$ Monte Carlo with $m_{top} = 160$ GeV/c^2; and d) dimuon events in $t\bar{t}$ Monte Carlo with $m_{top} = 160$ GeV/c^2. In all cases, only events where the leptons satisfy the p_T, fiducial, lepton identification, and isolation cuts are shown.

the $\not\!\!E_T$ vector is less than 50 GeV. Only jets with ${E_T}^{raw} > 10$ GeV and $|\eta| < 2.4$ are considered in the calculation of this angle. Figure 4.4 shows the distribution in the $\not\!\!E_T - \Delta\phi_{min}$ plane for $t\bar{t}$ Monte Carlo events generated with $m_{top} = 160$ GeV/c^2. Table 4.13 shows the efficiency of this cut for $t\bar{t}$ Monte Carlo events which pass the p_T, fiducial, lepton identification, isolation, and Z removal cuts.

m_{top}(GeV/c^2)	ee	$e\mu$	$\mu\mu$
100	0.786 ± 0.038	0.777 ± 0.019	0.791 ± 0.033
120	0.733 ± 0.038	0.741 ± 0.020	0.765 ± 0.030
140	0.810 ± 0.033	0.749 ± 0.018	0.774 ± 0.029
160	0.754 ± 0.034	0.747 ± 0.018	0.775 ± 0.027
180	0.783 ± 0.033	0.786 ± 0.017	0.786 ± 0.026
200	0.788 ± 0.031	0.762 ± 0.018	0.815 ± 0.025

Table 4.13: Combined efficiency of the $\not\!\!E_T$ magnitude and direction cuts for $t\bar{t}$ Monte Carlo events which pass the p_T, fiducial, lepton identification, isolation, and Z removal cuts.

4.5.3 Jet Cuts

For $m_{top} > 100$ GeV/c^2, we expect the b quarks in the final states of $t\bar{t}$ events to show up as jets in the detector. Requiring two jets will reduce all the major backgrounds, but should keep much of the signal. Figure 4.5 shows the ${E_T}^{raw}$ spectra of the highest ${E_T}^{raw}$ and second highest ${E_T}^{raw}$ jets with $|\eta| < 2.4$ in $t\bar{t}$ events, for $m_{top} = 120$ GeV/c^2 and $m_{top} = 180$ GeV/c^2. The spectra are quite different for the two top masses; the larger the top mass, the more p_T the b quarks receive. In this analysis, we require two jets with ${E_T}^{raw} > 10$ GeV and $|\eta| < 2.4$. The efficiency of the two-jet cut for events which pass all the previously listed cuts is shown in Table 4.14. Note that

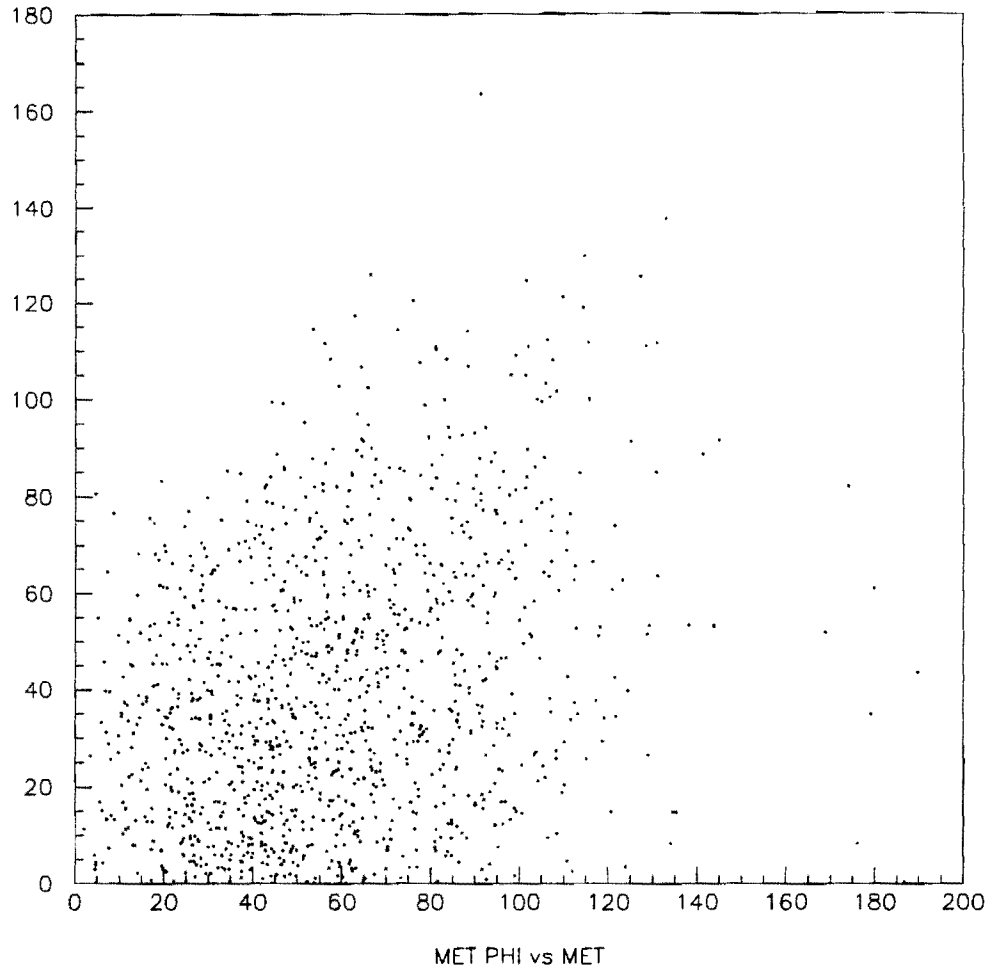

Figure 4.4: The plot of $\Delta\phi_{min}$ vs $\not\!\!E_T$ for $t\bar{t}$ Monte Carlo events generated with $m_{top} = 160$ GeV/c^2. The vertical axis is the angle between the $\not\!\!E_T$ vector and the nearest lepton or jet. The horizontal axis is the magnitude of the $\not\!\!E_T$ vector. Only events which pass the p_T, fiducial, lepton identification, isolation, and Z removal cuts are shown.

the efficiency is a strong function of the top mass, and falls off rapidly for $m_{top} < 120$ GeV/c^2.

m_{top}(GeV/c^2)	ee	$e\mu$	$\mu\mu$
100	0.432 ± 0.049	0.429 ± 0.026	0.419 ± 0.043
120	0.721 ± 0.045	0.690 ± 0.024	0.715 ± 0.037
140	0.830 ± 0.036	0.813 ± 0.019	0.867 ± 0.029
160	0.873 ± 0.033	0.895 ± 0.015	0.907 ± 0.023
180	0.889 ± 0.030	0.922 ± 0.013	0.913 ± 0.022
200	0.927 ± 0.025	0.957 ± 0.011	0.924 ± 0.021

Table 4.14: Efficiencies for $t\bar{t}$ Monte Carlo events to pass the two-jet requirement. These efficiencies are for events which pass the lepton p_T, fiducial, identification, isolation, Z removal, and $\not\!\!E_T$ (magnitude and direction) cuts.

4.5.4 Opposite Sign Cut

The final requirement in this search is that the two charged leptons have opposite sign of electric charge (*i.e.*, e^+e^-, $\mu^+\mu^-$, or $e^\pm\mu^\mp$). This requirement reduces background from W + jets production, where a hadronic jet is misidentified as an electron or muon, while keeping all of the $t\bar{t}$ signal events where both charged leptons come from the decay of a W, as the two W's in these events have opposite sign of electric charge. The efficiency of this cut, after all the other cuts have been applied is given in table 4.15. Table 4.16 gives the efficiency of the opposite sign cut after all other cuts except the two-jet cut have been applied. It can be seen from these tables that the opposite sign requirement is very efficient, but that it is more efficient at lower values of m_{top} than at higher values. The reason for this behavior is that the fraction of $t\bar{t}$ dilepton events where one of the leptons comes from the decay of a b quark increases slightly with m_{top}. Only half of the events with one lepton from W

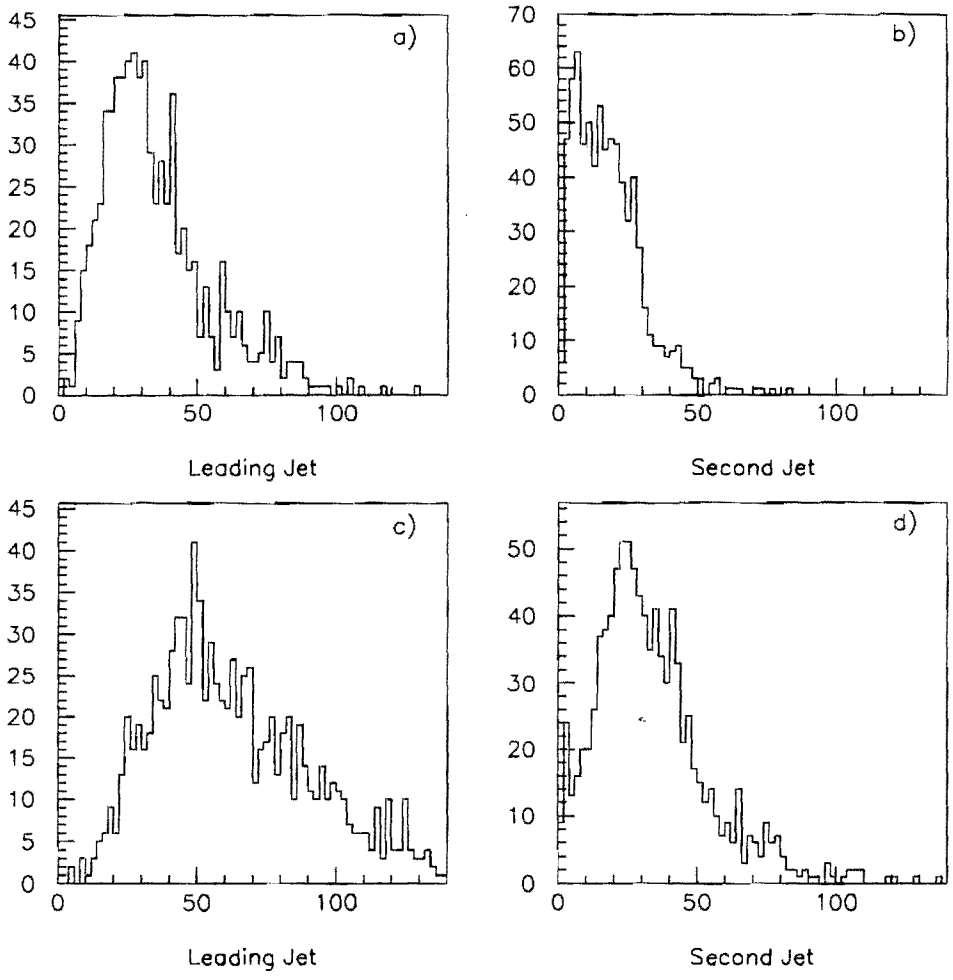

Figure 4.5: The E_T^{raw} spectra of jets with $|\eta| < 2.4$ in $t\bar{t}$ Monte Carlo events: a) leading jet in $m_{top} = 120$ GeV/c^2 Monte Carlo; b) next-to-leading jet in $m_{top} = 200$ GeV/c^2 Monte Carlo; c) leading jet in $m_{top} = 120$ GeV/c^2 Monte Carlo; d) next-to-leading jet in $m_{top} = 180$ GeV/c^2 Monte Carlo. E_T^{raw} is the uncorrected calorimeter E_T. Only events which pass the lepton p_T, fiducial, identification, isolation, Z removal, and $\not\!\!E_T$ and $\Delta\phi_{min}$ cuts are shown.

decay and the other from b or c decay will pass the opposite sign cut, and so the cut is less efficient at higher m_{top}. Of course, it is still 100% efficient for events where both leptons come from W decay, regardless of the value of m_{top}. The differences in the efficiencies of this cut for dielectron and dimuon events are not large compared to the statistical uncertainties, but may indicate that the contribution from b decay is slightly higher in the dimuon channel than in the dielectron channel (see Appendix B).

m_{top}(GeV/c^2)	ee	$e\mu$	$\mu\mu$
100	1.000 ± 0.034	0.989 ± 0.015	1.000 ± 0.028
120	1.000 ± 0.020	0.959 ± 0.015	0.962 ± 0.025
140	0.945 ± 0.028	0.949 ± 0.013	0.929 ± 0.026
160	0.908 ± 0.033	0.952 ± 0.012	0.932 ± 0.022
180	0.944 ± 0.026	0.949 ± 0.012	0.896 ± 0.025
200	0.952 ± 0.023	0.927 ± 0.014	0.931 ± 0.021

Table 4.15: Efficiency[41] of the opposite-sign cut for $t\bar{t}$ Monte Carlo events after all other cuts have been applied.

m_{top}(GeV/c^2)	ee	$e\mu$	$\mu\mu$
100	1.000 ± 0.015	0.995 ± 0.006	1.000 ± 0.012
120	1.000 ± 0.014	0.965 ± 0.011	0.968 ± 0.019
140	0.954 ± 0.024	0.950 ± 0.012	0.933 ± 0.023
160	0.913 ± 0.029	0.953 ± 0.011	0.938 ± 0.020
180	0.951 ± 0.023	0.953 ± 0.011	0.901 ± 0.023
200	0.949 ± 0.022	0.930 ± 0.013	0.928 ± 0.020

Table 4.16: Efficiency[41] of the opposite-sign cut for $t\bar{t}$ Monte Carlo events after all other cuts except the two-jet cut have been applied.

4.6 Overall Efficiency

Table 4.17 shows the overall efficiency after all cuts have been applied, and after folding in the trigger efficiencies found in Chapter 3. Table 4.18 gives the overall efficiency when all cuts except the two-jet cut are applied, again with the trigger efficiencies presented in Chapter 3 included.

m_{top}(GeV/c^2)	ee	$e\mu$	$\mu\mu$	Total
100	.0006 ± .0001	.0017 ± .0001	.0005 ± .0001	.0027 ± .0002
120	.0010 ± .0001	.0026 ± .0002	.0010 ± .0001	.0046 ± .0002
140	.0012 ± .0001	.0036 ± .0002	.0013 ± .0001	.0061 ± .0002
160	.0012 ± .0001	.0040 ± .0002	.0016 ± .0001	.0068 ± .0003
180	.0014 ± .0001	.0045 ± .0002	.0016 ± .0001	.0076 ± .0003
200	.0016 ± .0001	.0043 ± .0002	.0018 ± .0001	.0076 ± .0003

Table 4.17: Fractions of $t\bar{t}$ events which pass all the cuts of this analysis. The trigger efficiencies have been taken into account in the calculation of these numbers. The uncertainties are statistical only.

m_{top}(GeV/c^2)	ee	$e\mu$	$\mu\mu$	Total
100	.0013 ± .0001	.0038 ± .0002	.0013 ± .0001	.0064 ± .0002
120	.0013 ± .0001	.0038 ± .0002	.0015 ± .0001	.0066 ± .0002
140	.0015 ± .0001	.0044 ± .0002	.0015 ± .0001	.0074 ± .0003
160	.0014 ± .0001	.0045 ± .0002	.0017 ± .0001	.0076 ± .0003
180	.0016 ± .0001	.0049 ± .0002	.0018 ± .0001	.0083 ± .0003
200	.0017 ± .0001	.0044 ± .0002	.0019 ± .0001	.0081 ± .0003

Table 4.18: Fractions of $t\bar{t}$ events remaining after all cuts except for the two-jet cut have been applied. The trigger efficiencies have been taken into account in the calculation of these numbers. The uncertainties are statistical only.

4.7 Systematics

The uncertainties in the efficiencies given in the previous sections reflect the statistical uncertainty only. Potential sources of systematic uncertainty include the modeling of gluon radiation by the ISAJET Monte Carlo program, the simulation of the detector response by the QFL program, the set of structure functions used to generate the $t\bar{t}$ Monte Carlo samples, and the 10% uncertainty in the jet energy scale. In this section, we summarize the results of the studies of these systematics. These studies are described more fully in Reference [50].

We use the ISAJET Monte Carlo program to calculate the geometrical and kinematical acceptance. The acceptance depends on the choice of structure functions and the modeling of initial state radiation by ISAJET. The structure function uncertainty is estimated to be 2%. An estimate of the uncertainty due to the modeling of initial state radiation is found by comparing the acceptances to those obtained when gluon radiation is not permitted in the Monte Carlo generator. The combined systematic uncertainty in the acceptance is estimated to be 3%.

The number of Monte Carlo events which pass the lepton identification and isolation requirements depends on the modeling of initial state radiation by ISAJET and on simulation of the detector response by QFL. The uncertainties due to the radiation modeling are again found by removing gluon radiation in ISAJET, and are estimated to be 2% for the lepton identification cuts, and 1% for the isolation cuts. The uncertainties due to the simulation of the detector response are found by comparing to results obtained from an independent detector simulation program, and are estimated to be 5% for the lepton identification requirements and 1% for the isolation requirements. Re-

call that for leptons from Z boson decay, the differences in lepton identification efficiencies between data and Monte Carlo were approximately 5%. We take the total systematic uncertainty in the efficiency of the lepton identification requirement to be 6%, and the total systematic uncertainty in the efficiency of the isolation requirement to be 2%.

The calculation of $\not\!\!E_T$ depends on the measurement of the jet energies. We assign a 10% uncertainty to the jet energy scale. We vary the scale by $\pm 10\%$ to estimate the systematic uncertainty this introduces in the $\not\!\!E_T$ cuts and find it to be 2%.

The systematic uncertainty in the efficiency of the two-jet cut contains contributions from both the jet energy scale uncertainty and the modeling of gluon radiation by ISAJET. The systematic uncertainty in the efficiency of the two-jet cut depends on the top quark mass, and decreases with increasing m_{top}. Table 4.19 shows our estimates of the systematic uncertainties in the two-jet cut, found by varying the jet energy scale by $\pm 10\%$ and by removing gluon radiation in ISAJET. Table 4.19 also shows the total systematic uncertainty in the overall efficiency, which is the sum in quadrature of the individual systematic uncertainties.

m_{top} (GeV/c^2)	100	120	140	160	180	200
Two-jet cut (gluon radiation)	36	12	6	3	3	3
Tow-jet cut (energy scale)	5	4	2	1	1	1
All other cuts	8	8	8	8	8	8
Total	38	15	10	9	9	9

Table 4.19: Systematic uncertainty of the overall efficiency after all cuts have been applied, for several values of m_{top}. Also shown are the systematic uncertainties of the two-jet cut, and of all cuts except for the two-jet cut. All numbers refer to fractional uncertainties, expressed in percent.

We take the combined uncertainty in the overall efficiency to be the sum in quadrature of the statistical and systematic uncertainties. Table 4.20 shows the overall efficiency and the combined uncertainty for several values of m_{top}, both for the case where the two-jet requirement is imposed, and for the case where the two-jet requirement is not imposed.

m_{top} (GeV/c^2)	All cuts	All cuts except two-jet cut
100	.0027 ± .0010	.0064 ± .0005
120	.0046 ± .0007	.0066 ± .0006
140	.0061 ± .0006	.0075 ± .0007
160	.0068 ± .0007	.0076 ± .0007
180	.0076 ± .0007	.0083 ± .0007
200	.0076 ± .0007	.0081 ± .0007

Table 4.20: Overall detection efficiency for $t\bar{t}$ events. These numbers are the fractions of all $t\bar{t}$ events which will satisfy the cuts of this analysis, and are the sum of the ee, $e\mu$, and $\mu\mu$ channels. The efficiency is also shown for the case where the two-jet cut is relaxed. The uncertainties include both statistical and systematic contributions.

4.8 Results

We look through the dilepton data sample for events passing the cuts described in this chapter. Of the 87046 events in the sample, we find 992 which pass the p_T, fiducial, and lepton identification requirements. This number drops to 964 events after the isolation cuts are imposed. These 964 events are mostly $Z \rightarrow ll$ events. Only 4 of the 964 are $e\mu$ events. After applying the Z removal cut, we are left with 101 events: 50 ee, 47 $\mu\mu$, and 4 $e\mu$. The ee and $\mu\mu$ events are mostly from Drell-Yan production of lepton pairs. Requiring $\not\!\!E_T > 25$ GeV eliminates all of the ee and $\mu\mu$ events, leaving only

2 $e\mu$ events. Both of these events pass all the remaining cuts ($\not\!\!E_T$ direction, two-jets, and opposite sign of electric charge). Table 4.21 shows the number of events surviving as successive cuts are applied in 19.3 pb^{-1} of data. The two events which pass all the cuts will be described in more detail in Chapter 6.

Cut	ee	$e\mu$	$\mu\mu$	Total
p_T, Fiducial, Lepton ID	532	10	450	992
Isolation	525	4	435	964
Invariant Mass	50	4	47	101
$\not\!\!E_T$ magnitude	0	2	0	2
$\not\!\!E_T$ direction	0	2	0	2
Two jets	0	2	0	2
Opposite Sign	0	2	0	2

Table 4.21: The number of events surviving as successive cuts are applied in the data. The sample represents an integrated luminosity of 19.3 pb^{-1}.

Chapter 5

BACKGROUNDS

5.1 W Pair Production

The largest background to this search is from the pair production of W bosons, followed by the leptonic decay of each W. This yields a final state which has two isolated oppositely-charged leptons and two neutrinos, and which is very much like the $t\bar{t}$ events for which we are searching. The primary difference between the final states in $t\bar{t}$ and W pair events is that the former contain two b quarks, while the latter generally do not. The W pairs may be produced in association with two or more jets, in which case these events may fall into the signal region of this analysis.

In order to estimate the background from this process, we use the ISAJET Monte Carlo program to generate 50,000 $\bar{p}p \rightarrow W^+W^-$ events, and the QFL detector simulation program to model the detector response. Of the 50,000 events, 509 pass the fiducial, p_T, and lepton identification cuts. Recall that the branching ratio for each W to decay to e or μ is 2/9 (1/9 each for e and μ), so that the fraction of W pair events where both W's decay to electrons or

muons is approximately 5%. Table 5.1 shows the numbers of events surviving as the remaining cuts are successively applied. We find that 305 events pass all the cuts before the two-jet cut, and 44 events survive all the cuts, including the two-jet cut. From these numbers, we can calculate the fraction of W pair events lying in our signal region.

A next-to-leading-order (NLO) calculation [34] predicts the cross-section for the process $\bar{p}p \rightarrow W^+W^-$ to be 9.5 pb, while the cross-section returned from ISAJET is 6.0 pb. To predict the total number of W pair events in 19.3 pb^{-1}, we use the NLO result and assign a 30% uncertainty. The integrated luminosity of the Monte Carlo sample is thus 5300 pb^{-1}, about a factor of 270 higher than the data sample.

Using the NLO cross-section and the probability for a given W pair event to fall in the signal region found from the Monte Carlo, we estimate a background of 1.1 ± 0.3 events without the two-jet cut, and 0.16 ± 0.05 events with all cuts, including the two-jet cut in 19.3 pb^{-1} of data.

Cuts (cumulative)	ee	$e\mu$	$\mu\mu$	Total
p_T·Fid·ID	99	269	141	509
Isolation	99	265	139	503
Z Mass	76	265	99	440
$\not\!\!E_T$	56	177	72	305
Opposite Sign	56	177	72	305
Two-Jet	8	26	10	44

Table 5.1: Numbers of events from ISAJET W pair Monte Carlo surviving successive cuts, out of 50,000 generated events, corresponding to an integrated luminosity of approximately 5300 pb $^{-1}$.

5.2 Heavy Flavor

The process $\overline{p}p \rightarrow b\overline{b}$ or $c\overline{c}$ may produce events with two leptons if the b or c quarks decay semi-leptonically. If the heavy flavor quarks are produced in association with jets, these events may satisfy all the criteria of this analysis. In order to estimate the background from heavy flavor production, we use two independent Monte Carlo samples [43]. In addition to increasing the statistics available for this study, the use of two Monte Carlo samples allows us to check the results obtained from each against the other. Both samples use the ISAJET Monte Carlo program to generate the event, both use the CLEO [35] Monte Carlo program to decay the b quarks, and both use the QFL detector simulation program to simulate the detector response.

The first Monte Carlo sample contains events with at least one b quark with $p_T > 25$ GeV/c, and which contain at least two leptons (e or μ) passing p_T cuts explained below. ISAJET reports an integrated luminosity of 67.5 pb^{-1} for this sample. For the first 16.3 pb^{-1} of this sample, we require one lepton with $p_T > 14$ GeV/c and another with $p_T > 5$ GeV/c. For the remaining 51.2 pb^{-1}, we require that both leptons have $p_T > 10$ GeV/c. The first 16.3 pb^{-1} of this sample is needed to get the relative normalization between the Monte Carlo and the data. The lepton requirements were changed for the remaining 51.2 pb^{-1} in order to decrease the computing time needed to generate the sample.

The second sample contains events with at least two heavy flavor quarks (b, c, or t) each with $p_T > 12$ GeV/c, and two leptons each with $p_T > 5$ GeV/c. According to ISAJET, the integrated luminosity of this sample is 37.5 pb^{-1}. The value of m_{top} was set to 500 GeV/c^2 when generating the second sample, and the theoretical $t\bar{t}$ cross-section for the process $\overline{p}p \rightarrow t\bar{t}$ is

small enough at this top mass that there are no $t\bar{t}$ events in the Monte Carlo sample. After we require two 5 GeV/c leptons, approximately 7% of the events are $c\bar{c}$, the rest are $b\bar{b}$.

We do not rely on the cross-sections claimed by ISAJET for the estimate of the background. Instead, we normalize the Monte Carlo samples to the data by counting the numbers of $e\mu$ events in the data and Monte Carlo. Specifically, we look for $e\mu$ events where one of the leptons has $p_T > 18$ GeV/c and the other has $p_T > 7$ GeV/c. Table 5.2 lists the lepton identification cuts used to create this sample. We expect heavy flavor production to be the dominant source of events in this sample in the data, and therefore this will be a convenient control sample to which to normalize the Monte Carlo. Muon candidates are required to pass the matching requirements for hits in both the Central Muon System (CMU) and the Central Muon Upgrade system (CMP) chambers. The electron identification requirements are also somewhat more stringent than those used in the top search [44].

When counting the number of events in the normalization sample in the first Monte Carlo sample, we use only the first 16.3 pb^{-1}, as the lepton p_T requirements on the remaining 51.2 pb^{-1} already cut too hard on the second lepton. We estimate that both Monte Carlo samples lose 5% of the normalization events because of the p_T requirements on the heavy quarks. In the first sample, the $p_T > 25$ GeV/c requirement for at least one b quark keeps approximately 95% of the leptons with $p_T > 18$ GeV/c, while in the second sample, the $p_T > 12$ GeV/c requirement for at least two b, c, or t quarks keeps approximately 95% of the leptons with $p_T > 7$ GeV/c. As discussed in Chapter 3, the trigger efficiencies are approximately 92% for central electrons, and approximately 87% for muons with both CMU and CMP chamber hits. For

this background study, we use a rough value of $90\% \pm 5\%$ trigger efficiency for the normalization events in the data.

With these numbers, we can calculate equivalent luminosities, $\mathcal{L}_{equiv}$, for the two Monte Carlo samples by equating the cross-sections for normalization samples in the data and Monte Carlo samples. Table 5.3 shows the numbers of normalization events found in the two Monte Carlo samples and in the data, as well as $\mathcal{L}_{equiv}$, which has been scaled up by (67.5 pb^{-1}/16.3 pb^{-1}) for the first Monte Carlo sample to represent the entire sample. Note that less than 1% of the events in the normalization sample of the second Monte Carlo sample are from $c\bar{c}$ production, so it should be safe to use the first Monte Carlo sample, which ignored the $c\bar{c}$ contribution.

18 GeV/c Central Electron Cuts	7 GeV/c Central Electron Cuts
$E_T^{em} > 18$ GeV	$E_T^{em} > 7$ GeV
${p_T}^{track} > 13$ GeV/c	${p_T}^{track} > 3.5$ GeV/c
$E^{had}/E^{em} < 0.05$	$E^{had}/E^{em} < 0.05$
$E_T^{em}/{p_T}^{track} < 2$	$E_T^{em}/{p_T}^{track} < 2$
$\Delta x < 1.5$ cm	$\Delta x < 1.5$ cm
$\Delta z < 3.0$ cm	$\Delta z < 3.0$ cm
$L_{shr} < 0.2$	$L_{shr} < 0.2$
$\chi^2_{strip} < 10$	$\chi^2_{strip} < 15$
18 GeV/c Muon Cuts	**7 GeV/c Muon Cuts**
${p_T}^{track} > 18$ GeV/c	${p_T}^{track} > 7$ GeV/c
$E^{em} < 2$ GeV	$E^{em} < 2$ GeV
$E^{had} < 6$ GeV	$E^{had} < 6$ GeV
$E^{em} + E^{had} > 0.1$ GeV	$E^{em} + E^{had} > 0.1$ GeV
$d_0 < 3$ mm	$d_0 < 3$ mm
$\Delta z^{vrt-trk} < 5$ cm	$\Delta z^{vrt-trk} < 5$ cm
CMU and CMP matches	CMU and CMP matches

Table 5.2: Selection criteria for electrons and muons used to normalize the $b\bar{b}$ Monte Carlo samples.

	Data	Monte Carlo 1	Monte Carlo 2
N_{norm}	45	34	125
$\mathcal{L}_{equiv}$ pb^{-1}	19.3	57 ± 13	51 ± 9

Table 5.3: Numbers of events in the normalization samples, N_{norm}, in the data and in the two Monte Carlo samples. For the data, $\mathcal{L}_{equiv}$ is the integrated luminosity of the 1992-1993 run, 19.3 pb^{-1}. For the first Monte Carlo sample, $\mathcal{L}_{equiv}$ has been scaled up by the ratio (67.5 pb^{-1}/16.3 pb^{-1}) so that it represents the entire sample.

Knowing the relative normalizations of the two Monte Carlo samples to the data, it would seem a straightforward matter to count the number of events in the signal region, and to use that number to estimate the expected background from heavy flavor production. There are no events in either Monte Carlo sample which lie in the signal region of this analysis. This allows us to set upper limits (at 68% CL) of 0.37 events and 0.42 events from the first and second samples, respectively. When the results from the two samples are combined, the upper limit drops to 0.20 events. Ideally, we would like to have larger Monte Carlo samples to look at, but it took several months of computer time to generate each of the two samples we are using, and larger samples are just not available.

In an effort to set a better upper limit on the expected background, we use the Monte Carlo samples to predict the number of heavy flavor events which pass all of the analysis cuts except for the $\not\!\!E_T$ (magnitude and direction) and two-jet cuts, and then multiply this number by a rejection factor for the $\not\!\!E_T$ cuts, also obtained from the Monte Carlo. Table 5.4 shows the numbers of events in the Monte Carlo samples which pass the fiducial, lepton identification, isolation, Z removal, and opposite sign requirements detailed in Chapter 4. That is, they pass the full set of cuts except that the $\not\!\!E_T$ (magnitude and

direction) and two-jet cuts have been removed. Also shown in Table 5.4 are the numbers of Monte Carlo events which pass all the analysis cuts except for the $\not\!\!E_T$ and two-jet cuts, but where the leptons have the same sign of electric charge. Using these numbers, we can predict the number of heavy flavor events in the data. These predictions appear in Table 5.5. The p_T requirements on heavy quarks for the two Monte Carlo samples are essentially 100% efficient for events where both leptons have $p_T > 15$ GeV/c, and the trigger efficiency is also very nearly 100% for these events, so we need not correct for these effects as we did before with the normalization sample. The fraction of events in the second Monte Carlo sample with two leptons each with $p_T > 15$ GeV/c which are from $c\bar{c}$ production is less than 1%, leading us to conclude again that the $c\bar{c}$ contribution is negligible and that it is appropriate to use both Monte Carlo samples to estimate the heavy flavor background.

We use the Monte Carlo samples to estimate a rejection factor for the $\not\!\!E_T$ cuts. The rejection factor is found from events with the lepton p_T thresholds lowered to 15 GeV/c and which pass the fiducial, lepton identification, isolation, Z removal, and opposite sign requirements. That is, we use the 35 events found in the first Monte Carlo sample when the lepton p_T threshold is 15 GeV/c, and the 50 events found in the second Monte Carlo sample. None of these events in either Monte Carlo sample passes the $\not\!\!E_T$ cuts, allowing us to set upper limits (68% CL) of 0.031 from the first sample, 0.022 from the second sample, and 0.013 when the samples are combined. We can multiply these $\not\!\!E_T$ cut rejection factors by the appropriate numbers in Table 5.5 to set upper limits on the heavy flavor background. Table 5.6 gives the estimated background due to heavy flavor production, before the two-jet cut is applied.

Lepton p_T Threshold	Monte Carlo 1	Monte Carlo 2	Combined
20 GeV/c	3	4	7
15 GeV/c	35	50	85
20 GeV/c	2	2	4
15 GeV/c	11	7	18

Table 5.4: Numbers of events found in the two Monte Carlo samples with the $\not\!\!E_T$ and two-jet cuts removed. The upper two rows are events in which the leptons have opposite sign of electric charge. The lower two rows are events in which the leptons have the same sign of electric charge.

Lepton p_T Threshold	Monte Carlo 1	Monte Carlo 2	Combined
15 GeV/c, Opp Sign	11.8 ± 3.3	19.0 ± 4.2	15.2 ± 2.7
20 GeV/c, Opp Sign	1.0 ± 0.6	1.5 ± 0.8	1.3 ± 0.5
15 GeV/c, Same Sign	3.7 ± 1.4	2.7 ± 1.1	3.2 ± 0.9
20 GeV/c, Same Sign	0.7 ± 0.5	0.8 ± 0.6	0.7 ± 0.4

Table 5.5: Expected numbers of heavy flavor events in 19.3 pb^{-1} of data, for lepton p_T thresholds of 15 and 20 GeV/c, after all cuts have been applied except for the $\not\!\!E_T$ and two-jet cuts. The upper two rows are events in which the leptons have opposite sign of electric charge. The lower two rows are events in which the leptons have the same sign of electric charge.

5.3 $\tau^+\tau^-$

Drell-Yan [46] production of $\tau^+\tau^-$ pairs can lead to final states with two leptons and $\not\!\!E_T$. If both sides decay leptonically ($\tau \to \ell\nu\overline{\nu}$), the final state will contain two charged leptons of opposite sign, and four neutrinos which may provide $\not\!\!E_T$. If the τ pairs are produced in association with jets, these events may well satisfy the selection criteria of this analysis. We can express the expected background from this process, $N^{\tau\tau}$, as

$$N^{\tau\tau} = \mathcal{L}\,\sigma(\overline{p}p \to \tau^+\tau^-)\,BR^2\,\epsilon^{\tau\tau}_{p_T\text{-}Fid\text{-}ID\text{-}Iso\text{-}OS}\,\epsilon^{\tau\tau}_{topology}$$

Lepton p_T Threshold	Monte Carlo 1	Monte Carlo 2	Combined
15 GeV/c	$0.00^{+.37}_{-.00}$	$0.00^{+.42}_{-.00}$	$0.00^{+.20}_{-.00}$
20 GeV/c	$0.00^{+.03}_{-.00}$	$0.00^{+.03}_{-.00}$	$0.00^{+.02}_{-.00}$

Table 5.6: Expected background from heavy flavor production in 19.3 pb^{-1} of data, for lepton p_T thresholds of 15 and 20 GeV/c, after all cuts have been applied except for the two-jet cut.

where is the integrated luminosity, $\sigma(\bar{p}p \rightarrow \tau^+\tau^-)$ is the $\tau^+\tau^-$ production cross-section, BR is the branching ratio for a single τ to decay leptonically, $\epsilon^{\tau\tau}_{p_T \cdot Fid \cdot ID \cdot Iso \cdot OS}$ is the combined efficiency of the fiducial, p_T, lepton identification, isolation, and opposite sign cuts, and $\epsilon^{\tau\tau}_{topology}$ is the combined efficiency of the mass, $\not\!\!E_T$ magnitude and direction, and two-jet requirements.

The expected background from this process depends strongly on the jet activity in the events. In order to correctly model the jet production in Drell-Yan events, we turn to the data rather than trust the predictions of a Monte Carlo program. To do this, we start with the e^+e^- events in the data which pass the fiducial, p_T, electron identification and isolation cuts described in Chapter 4. As can be seen from Figure 4.3, approximately 90% of these e^+e^- pairs come from the decay of the Z boson. The remaining 10% lie in the mass continuum away from the Z pole.

For each of these e^+e^- events, we replace each electron with a τ with the same momentum [45]. Each τ is decayed by ISAJET, and the decay products are simulated by QFL. The τ's are forced to decay leptonically. The output of this simulation is merged back into the original event, in place of the original electrons. We define $\epsilon^{\tau\tau}_{topology}$ to be the number of these simulated events passing all the cuts of the analysis, divided by the number of simulated events passing just the fiducial, p_T, lepton identification, isolation, and oppo-

site sign cuts. That is, $\epsilon^{\tau\tau}_{topology}$ is the efficiency of the mass, $\not\!\!E_T$ magnitude and direction, and two-jet cuts for $\tau^+\tau^-$ which satisfy all the other requirements. In order to boost statistics, we use each e^+e^- parent event 50 times, resulting in 50 different, albeit correlated, daughter events. We use 525 e^+e^- parent events, and after decaying and simulating them 50 times each, we find 1535 events passing the fiducial, p_T, lepton identification, isolation, and opposite sign requirements. Of these 1535, 18 pass the topology cuts. The 18 events are from only 3 parent events. One parent event contributes 15 daughters passing the topology cuts, the second contributes 2 daughters passing the topology cuts, and the third contributes 1 daughter passing the topology cuts. We take the uncertainty in the 18 events to be $15 \oplus 2 \oplus 1 = 15.2$ events, and so we find $\epsilon^{\tau\tau}_{topology} = .012 \pm .011$. Before the two-jet cut is applied, there are 30 of the simulation events surviving, yielding an efficiency of $.020 \pm .010$ without the two-jet cut.

It should be noted that the 525 dielectron parent events used in this study may not all be from Drell Yan production of e^+e^- pairs. There may in fact be some events from the process $t\bar{t} \rightarrow e^+e^-\nu_e\bar{\nu_e}b\bar{b}$ in the 525 events. These 525 events are used to determine the rejection factor of the event topology cuts, and the presence of $t\bar{t}$ events may lead to an underestimate of this rejection factor, as the event topology cuts were designed to keep $t\bar{t}$ events. This in turn may lead to an overestimate of the background from Drell-Yan production of $\tau^+\tau^-$ pairs. However, we find no dielectron events and only 2 events total (both $e\mu$) in the data which satisfy the selection criteria of this analysis. Assuming that the two observed signal events are from $t\bar{t}$ production, and using the efficiency of the Z removal cuts for $t\bar{t}$ dilepton events, we estimate 0.1 $t\bar{t}$ events in the dielectron channel which fail the Z removal cut but pass all the other cuts. This is certainly a negligible number when compared to the 525 dielectron

events that we use, but it is perhaps more appropriate to compare it to the number of parent events that produce daughters which pass the topology cuts. As mentioned in the previous paragraph, the 18 events passing the topology cuts are from only 3 parents, with one of the parents producing 15 of the 18 events. If this event is really a $t\bar{t}$ event, then we have overestimated the $\tau^+\tau^-$ background considerably. Again, we note that we expect only 0.1 $t\bar{t}$ events in this background sample, and we use all 18 events passing the topology cuts to estimate the background, with the awareness that we may be overestimating it.

We use the ISAJET Monte Carlo program to calculate $\epsilon^{\tau\tau}_{p_T \cdot Fid \cdot ID \cdot Iso \cdot OS}$, since this number is fairly insensitive to the associated jet activity. We generate 100,000 Drell-Yan $\tau^+\tau^-$ events in the mass window (50 GeV/c^2, 500 GeV/c^2), and force the τ's to decay leptonically. We expect this mass window to be quite safe in that it keeps essentially all of the $\tau^+\tau^-$ events whose daughter leptons pass the p_T cuts. Of the 100,000 Monte Carlo events, we find 248 ee, 339 $\mu\mu$, and 699 $e\mu$ events passing the fiducial, p_T, lepton identification, isolation, and opposite sign cuts, and so we take $\epsilon^{\tau\tau}_{p_T \cdot Fid \cdot ID \cdot Iso \cdot OS} = 0.0129 \pm 0.0004$.

The integrated luminosity of the run is $\mathcal{L} = 19.3 \pm 0.7 pb^{-1}$ [10]. We take the branching ratio for a single τ to decay leptonically to be $BR = (.357 \pm .003)$, so $BR^2 = .127 \pm .002$ [36].

To find the production cross-section, we start with the published value of $\sigma(\bar{p}p \rightarrow Z \rightarrow e^+e^-) = 0.209 \pm 0.021$ nb [37]. Assuming lepton universality and ignoring the electron and tau mass difference, the cross section for the process $\sigma(\bar{p}p \rightarrow Z \rightarrow \tau^+\tau^-)$ will be the same. This published value of the cross-section must be modified to take into account three effects. First, the full matrix element for this Drell-Yan process will include contributions from

the Z and from the photon. This means that the cross section will include a Z^2 term, a $Z\gamma$ interference term, and a γ^2 term. The published cross-section is for just the Z^2 piece, and so needs to be corrected for the interference and photon contributions. Second, when we found $\epsilon^{\tau\tau}_{p_T \cdot Fid \cdot ID \cdot Iso \cdot OS}$, we limited the mass range to (50 GeV/c^2, 500 GeV/c^2). While this was safe because it kept all the events which might pass the cuts, we need to use a production cross-section for just that mass range when calculating the expected background. Third, the published $\sigma(\bar{p}p \rightarrow Z \rightarrow e^+e^-)$ cross-section is normalized to a different total cross-section $\sigma(\bar{p}p \rightarrow X)$ than was used to determine the integrated luminosity, and must be scaled up by a factor of 1.11. Taking all three of these corrections into account, we arrive at a value of 0.246 ± 0.025 nb for the process $\sigma(\bar{p}p \rightarrow \tau^+\tau^-)$.

Multiplying all the terms together gives us an expected background of 0.151 ± 0.079 events without the two-jet cut, and $N^{\tau\tau} = 0.090 \pm 0.076$ events after all cuts have been applied. Table 5.7 shows the expected number of background events from Drell-Yan production of tau pairs, before and after the two-jet cut is applied, and broken down into ee, $\mu\mu$, and $e\mu$ cases separately.

Cuts	ee	$\mu\mu$	$e\mu$	Total
Before two-jet	0.029 ± 0.015	0.040 ± 0.021	0.082 ± 0.043	0.151 ± 0.079
All cuts	0.017 ± 0.015	0.024 ± 0.020	0.049 ± 0.042	0.090 ± 0.076

Table 5.7: Expected number of background events from Drell-Yan production of $\tau^+\tau^-$ pairs. Numbers are given for the expected background after all cuts have been applied, and also for the expected background after all cuts have been applied except for the two-jet cut.

5.4 Hadron Misidentification

Hadronic particles can sometimes look very much like leptons in the CDF detector. This can happen, say, if a charged hadron punches through the calorimeters without interacting significantly before reaching the muon chambers. In this case, we would see a CTC track pointing towards hits in a muon chamber, with very little energy deposited in the calorimeters. This is how we would expect a real muon to appear in the detector. Charged pions and kaons may decay to muons before reaching the calorimeters, and so may be misidentified as muons from the primary interaction. Charged hadrons showering very early in the calorimeters leave most of their energy in the CEM calorimeter. This may happen through the charge exchange process (*e.g.*, $\pi^+ + n \rightarrow \pi^0 + p$ or $\pi^- + p \rightarrow \pi^0 + n$), and the photons from the π^0 decay deposit all their energy in the CEM calorimeter. In this case, we would see a charged track pointing towards a predominantly electromagnetic cluster, and we might misidentify the hadron as an electron. Charged hadrons which have π^0's nearby will produce tracks which point at electromagnetic energy, and may be misidentified as electrons.

Because the probability of misidentifying a hadron as a lepton is small ($\approx 10^{-4}$), we can neglect the potential background from the case where two hadrons in the same event fake leptons, and concentrate on the case where there is one real lepton in the event, plus a hadron which fakes a second lepton. We expect the only non-negligible source of such events to be W events where there are jets produced along with the W, and where the W decays leptonically.

In order to estimate the background from misidentified hadrons in $W \rightarrow \ell\nu$ events, we note that we expect the charge of the faked lepton to be uncorrelated with the charge of the W, and so we should see on average,

as many same-sign events as opposite-sign events. We then look through the data for same-sign events which pass all the other cuts except for the two-jet cut. We find no same-sign events. This allows us to set a limit (68% CL) of 1.1 events from hadron misidentification before the two-jet cut is applied.

We calculate a rejection factor for the two-jet cut by looking at the jet multiplicities in W events. Specifically, we select $W \rightarrow e\nu$ events which pass the $\not\!\!E_T$ magnitude and direction cuts of the analysis, after the jets in the event have been corrected. We consider jets which have corrected $p_T > 20$ GeV/c and $|\eta| < 1.2$ to be candidates for faking leptons. There are 840 such jets in the W events. We then ask how many of these jets are in events containing at least two other jets with uncorrected $p_T > 10$ GeV/c and $|\eta| < 2.4$, and we find 118 such jets. This gives us a rejection factor for the two-jet cut of 118/840 or 0.140 ± 0.014. After applying this rejection factor to the number of fake events before the two-jet cut, we find an upper limit (68% CL) on the expected background due to hadron misidentification of 0.15 events.

As a check of this result, we have estimated the probabilities that a hadron jet gets misidentified as a lepton by looking at a sample of jet data. When these fake rate probabilities are multiplied by the appropriate numbers of jets present in W events, we find an expected number of background events due to fakes of 0.06 ± 0.04 events, in good agreement with the upper limit of 0.15 events presented above.

5.5 Drell-Yan Production of Lepton Pairs

Drell-Yan production of dielectron and dimuon events can result in events which pass all the cuts of this analysis. In order for this to happen, there must be at least two jets produced along with the ee or $\mu\mu$ pair, and the

leptons and jets must be mismeasured in such a way that the event as a whole passes the $\not\!\!E_T$ magnitude and direction requirements. Of course, dielectron and dimuon events where the dilepton invariant mass is between 75 GeV/c^2 and 105 GeV/c^2 are rejected as possible Z events, so only events in the continuum outside the the Z mass window contribute to the background.

This background depends strongly on the jet activity in the Drell-Yan events, and on the detector response. Rather than rely on Monte-Carlo estimates of these quantities, we use the $Z \rightarrow ee, \mu\mu$ data to find rejection factors for the two-jet and $\not\!\!E_T$ cuts, and apply these rejection factors to the number of dielectron and dimuon events which lie outside the Z mass window. Table 5.8 shows the numbers of dielectron and dimuon events surviving the $\not\!\!E_T$ and two-jet cuts. There are a total of 863 events inside the Z mass window. Only 1 of these events passes the combined $\not\!\!E_T$ and two-jet cuts. There are 97 events outside of the Z mass window. Simple multiplication of these numbers yields an expected background of 0.11 ± 0.11 events. There are 2 Z events which pass all cuts except for the two-jet cut. This yields an expectation of 0.22 ± 0.16 Drell-Yan events passing all the cuts except for the the-jet cut. Higher mass Drell-Yan events contain, on average, more jet activity than do lower mass events. We correct for this effect by using a boson + 2 jet matrix element calculation [38]. We find that the events below the Z mass window are 71% as likely to pass the two-jet cut as are events inside the Z mass window, and events above the Z mass window are 1.34 times as likely to pass the two-jet cut as the events inside the Z mass window. Weighting the events outside of the Z mass window by their appropriate correction factors results in an overall correction of .89, and so the expected Drell-Yan background is $.10 \pm .10$ events.

It should be noted here that the single Z event which passes all the

Cuts	$M_{ll} < 75$	$75 < M_{ll} < 105$	$105 < M_{ll}$
		ee	
No $\not\!\!E_T$ or two-jet	38	475	12
$\not\!\!E_T$ only	0	1	0
Two-jet only	2	21	1
$\not\!\!E_T$ and two-jet	0	0	0
		$\mu\mu$	
No $\not\!\!E_T$ or two-jet	31	388	16
$\not\!\!E_T$ only	0	1	0
Two-jet only	3	18	1
$\not\!\!E_T$ and two-jet	0	1	0
		$e\mu$	
No $\not\!\!E_T$ or two-jet	69	863	28
$\not\!\!E_T$ only	0	2	0
Two-jet only	5	39	2
$\not\!\!E_T$ and two-jet	0	1	0

Table 5.8: Numbers of dielectron and dimuon events passing the $\not\!\!E_T$ (magnitude and direction) cuts and the two-jet cuts. These numbers are for events which pass the p_T, fiducial, lepton identification, isolation, and opposite-sign cuts. All masses are in GeV/c^2

cuts is quite possibly a $t\bar{t}$ event. This event (run 43170, event 198920) contains two muons, two jets, and large $\not\!\!E_T$ which does not point near either the muons or jets. One of the jets has an identified secondary vertex, which suggests that this jet contains a b quark. If this really is a $t\bar{t}$ event, then we have probably overestimated the Drell-Yan background. Using the fact there are only 2 events in the data which pass all the selection criteria of this analysis, we estimate 0.2 $t\bar{t}$ events which fail the Z removal cut but which pass all the other cuts. There is an 18% chance that 0.2 events expected fluctuates up to 1 or more events observed, so we certainly cannot rule out the chance that the

Cuts (cumulative)	ee	$\mu\mu$	Total
Before two-jet	$.10 \pm .07$	$.10 \pm .07$	$.20 \pm .10$
All cuts	$.05 \pm .05$	$.05 \pm .05$	$.10 \pm .10$

Table 5.9: Expected number of background events from Drell-Yan production of lepton pairs, shown for all cuts except the two-jet cut, and after all cuts have been applied.

event in question is from $t\bar{t}$ production. We keep this event when calculating this background, with the knowledge that we may be making an overestimate.

Table 5.9 shows the expected numbers of background events from Drell-Yan dielectron and dimuon production with and without the two-jet cut.

5.6 Summary

Table 5.10 summarizes the estimates of the backgrounds. We see the expectation for the total background is 1.5 ± 1.2 events before the two-jet cut, and 0.35 ± 0.21 events after all cuts.

Source	Background before two-jet cut	Background after all cuts
	ee	
WW	0.21 ± 0.06	0.03 ± 0.01
$b\bar{b}$	$0.00^{+0.03}_{-0.00}$	$0.00^{+0.03}_{-0.00}$
$\tau\tau$	0.03 ± 0.02	0.02 ± 0.02
Fakes	$0.0^{+1.1}_{-0.0}$	$0.00^{+0.15}_{-0.00}$
Drell-Yan	0.10 ± 0.07	0.05 ± 0.05
Total	0.34 ± 1.1	0.10 ± 0.16
	$\mu\mu$	
WW	0.26 ± 0.08	0.04 ± 0.01
$b\bar{b}$	$0.00^{+0.03}_{-0.00}$	$0.00^{+0.03}_{-0.00}$
$\tau\tau$	0.04 ± 0.02	0.02 ± 0.02
Fakes	$0.0^{+1.1}_{-0.0}$	$0.00^{+0.15}_{-0.00}$
Drell-Yan	0.10 ± 0.07	0.05 ± 0.05
Total	0.40 ± 1.1	0.11 ± 0.16
	$e\mu$	
WW	0.65 ± 0.19	0.10 ± 0.03
$b\bar{b}$	$0.00^{+0.03}_{-0.00}$	$0.00^{+0.03}_{-0.00}$
$\tau\tau$	0.08 ± 0.04	0.05 ± 0.04
Fakes	$0.0^{+1.1}_{-0.0}$	$0.00^{+0.15}_{-0.00}$
Total	0.73 ± 1.1	0.15 ± 0.16
	$ee + \mu\mu + e\mu$	
WW	1.1 ± 0.3	0.16 ± 0.05
$b\bar{b}$	$0.0^{+0.03}_{-0.00}$	$0.00^{+0.03}_{-0.00}$
$\tau\tau$	0.2 ± 0.1	0.09 ± 0.08
Fakes	$0.0^{+1.1}_{-0.0}$	$0.0^{+0.15}_{-0.00}$
Drell-Yan	0.2 ± 0.2	0.10 ± 0.10
Grand Total	1.5 ± 1.2	0.35 ± 0.21

Table 5.10: Expected numbers of background events from various sources.

Chapter 6

RESULTS

6.1 Description of the Signal Events

As can be seen from Table 4.21, the data contain two events surviving the p_T, fiducial, lepton identification, isolation, Z removal, and $\not\!\!E_T$ magnitude cuts. Both of these events contain an electron and a muon, and both pass all the remaining cuts: $\not\!\!E_T$ direction, two-jet, and opposite sign of electric charge requirements.

6.1.1 The DPF Event

The first of the two signal events is usually referred to as the DPF event, due to the fact that it was recorded in late October of 1992, just before the Division of Particles and Fields (DPF) conference at Fermilab that year. It is event number 127085 of run 41540. The event contains an electron, a muon, and three jets. Two of the jets satisfy the ${E_T}^{raw}$ and η requirements of the two-jet cut. Table 6.1 summarizes the information for this event. Figures 6.1 and 6.2 show the tracking and calorimeter displays for this event.

The muon in this event is very close to the boundary in ϕ between two central calorimeter wedges. Because of scattering, we do not know the exact path the muon took on its way out to the CMP chamber. When we propagate the CTC track out through the calorimeters, taking into account the magnetic fields therein, we find that the most likely case has the muon passing through the the CEM at a distance of about 0.2 cm from the edge of the active region. The track would not pass through the active region of the CHA and would also miss the CMU chambers. We see no CMU chamber hits for the muon. There are hits in three of the four layers of the CMP muon chamber. These hits are very well matched (0.09 cm) to the extrapolated track position. One may use the muon chamber hits to estimate the angle through which the muon passed through the chamber. The agreement between this angle and the angle of the extrapolated track is poor, but within the large tail of the distribution measured in $W \rightarrow \mu\nu$ events. Note that this is not a quantity that we use for muon identification in this analysis, due to its low efficiency. The energies deposited in the CEM and CHA towers nearest the projected path of the muon are 1.3 GeV and 1.6 GeV, respectively.

We have run the JETVTX [10] vertexing algorithm to search for secondary vertices in this event. We find that Jet 1 in Table 6.1 has a secondary vertex at a distance of 0.047 ± 0.004 cm from the beam line, indicating that it is most likely a b quark jet. The JETVTX algorithm is expected to be approximately $22\% \pm 6\%$ efficient at finding at least one secondary vertex in $t\bar{t}$ events with three or more observed jets for $m_{top} > 120$ GeV/c^2 [10]. The probability of finding a secondary vertex in non-heavy flavor jets is approximately 1% [10].

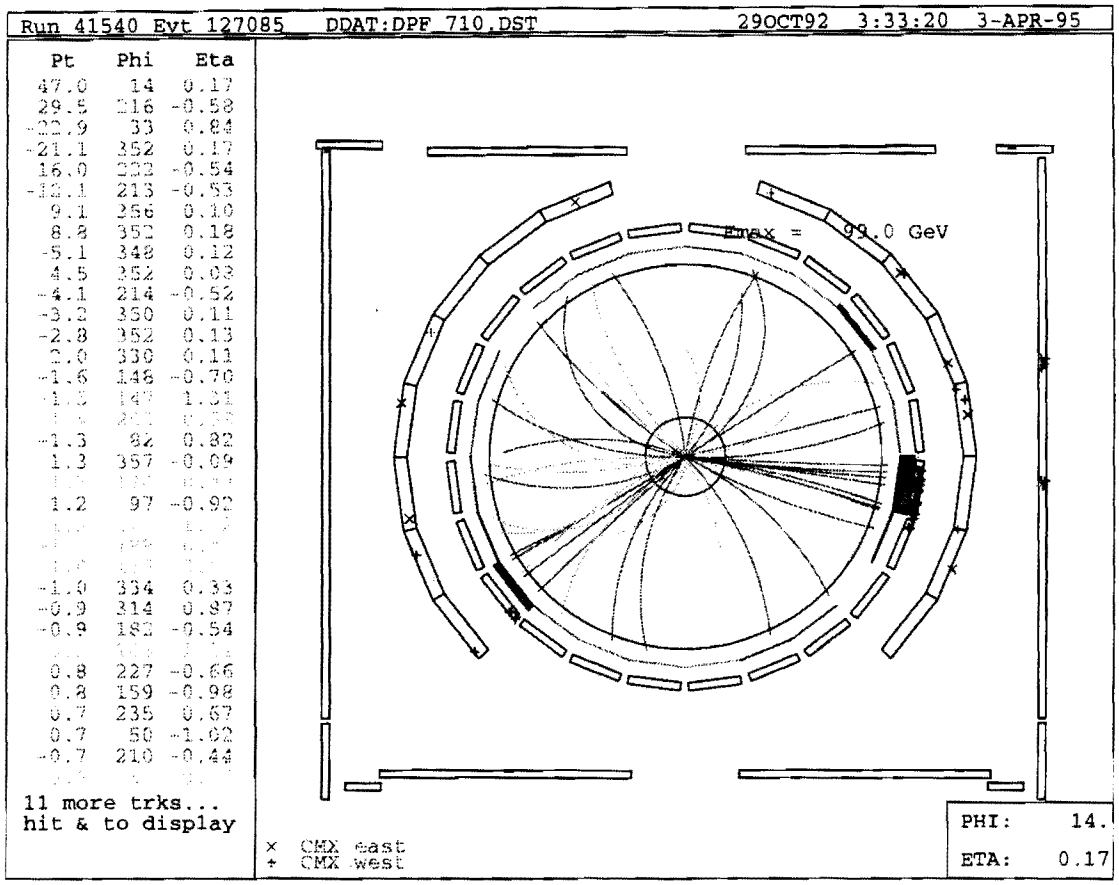

Figure 6.1: The CTC event display for the DPF event. This is a view looking down the beamline. The muon track is at $\phi = 14°$, and the electron track is at $\phi = 32°$. Also visible are two large jets at $\phi = 352°$ and $\phi = 215°$. The central calorimeter energy depositions are shown, with the darker shading indicating the electromagnetic energy, and the lighter shading indicating the hadronic energy. Further out in radius are the hits in the CMU, CMX, and CMP chambers.

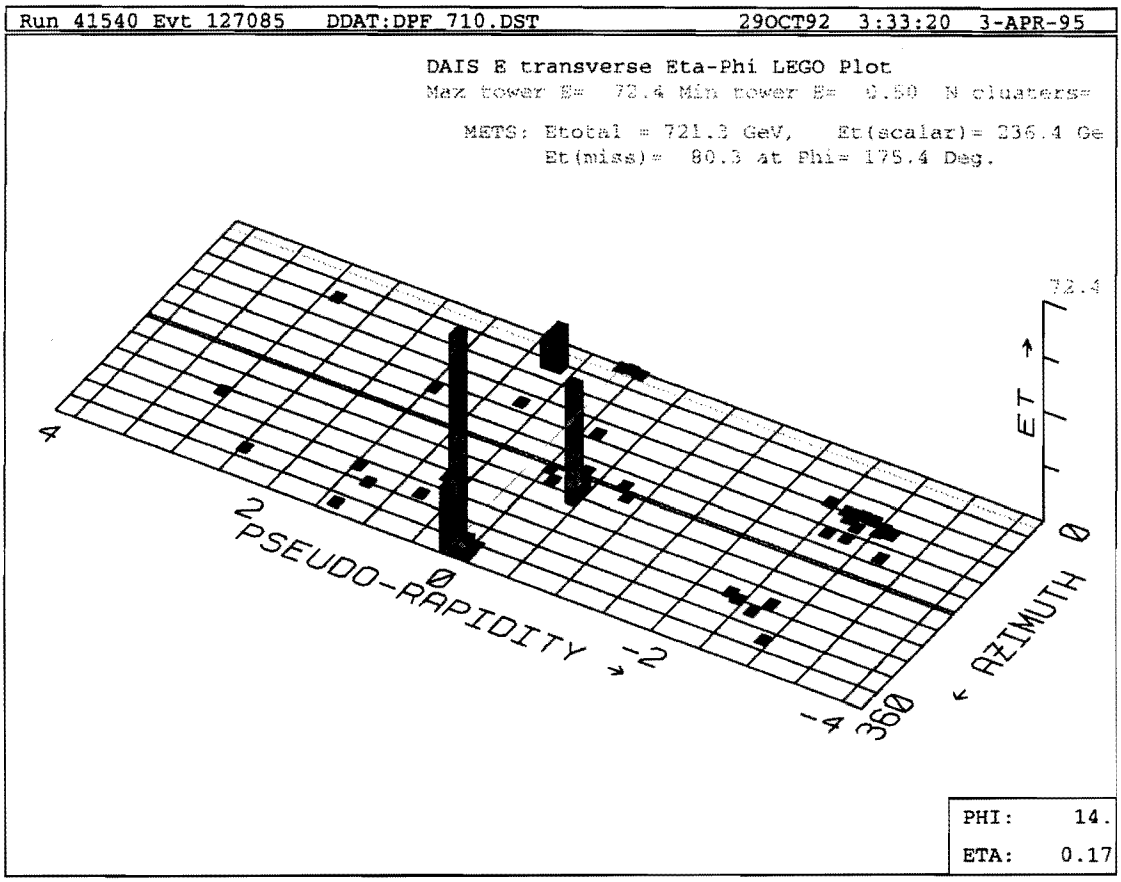

Figure 6.2: The calorimeter event display for the DPF event. The darker shading represents energy in the electromagnetic calorimeters, and the lighter shading represents energy in the hadronic calorimeters.

Object	p_T (GeV/c) before jet corrections	p_T (GeV/c) after jet corrections	η	ϕ
e^-		22.0	0.84	32°
μ^+		47.5	0.17	14°
Jet 1	107.9	131	0.11	352°
Jet 2	44.3	61	−0.54	215°
Jet 3	18.0	26	−2.94	112°
$\not\!\!E_T$		136		179°

Table 6.1: Properties of the DPF event. The energy corrections for Jet 1 and Jet 2 have been done assuming that they are b quark jets. The energy correction for Jet 3 has been done assuming that it is a light quark or gluon jet.

6.1.2 The CEMX Event

The second of the two signal events is sometimes called the CEMX event because it contains a central electron and a muon with hits in the CMX chambers. It is event number 38382 of run 47122. In addition to the electron and muon, there are three jets in the event. Two of these jets satisfy the E_T^{raw} and η requirements of the two-jet cut. Table 6.2 summarizes the information for this event. Figures 6.3 and 6.4 show the tracking and calorimetry displays. Two of the jets pass through the SVX. We use the JETVTX algorithm to search for secondary vertices in these jets. No secondary vertices are found in this event.

6.2 Conclusions

We observe 2 events in the signal region, with an expected background of 0.35 ± 0.21 events. The probability for this background to fluctuate

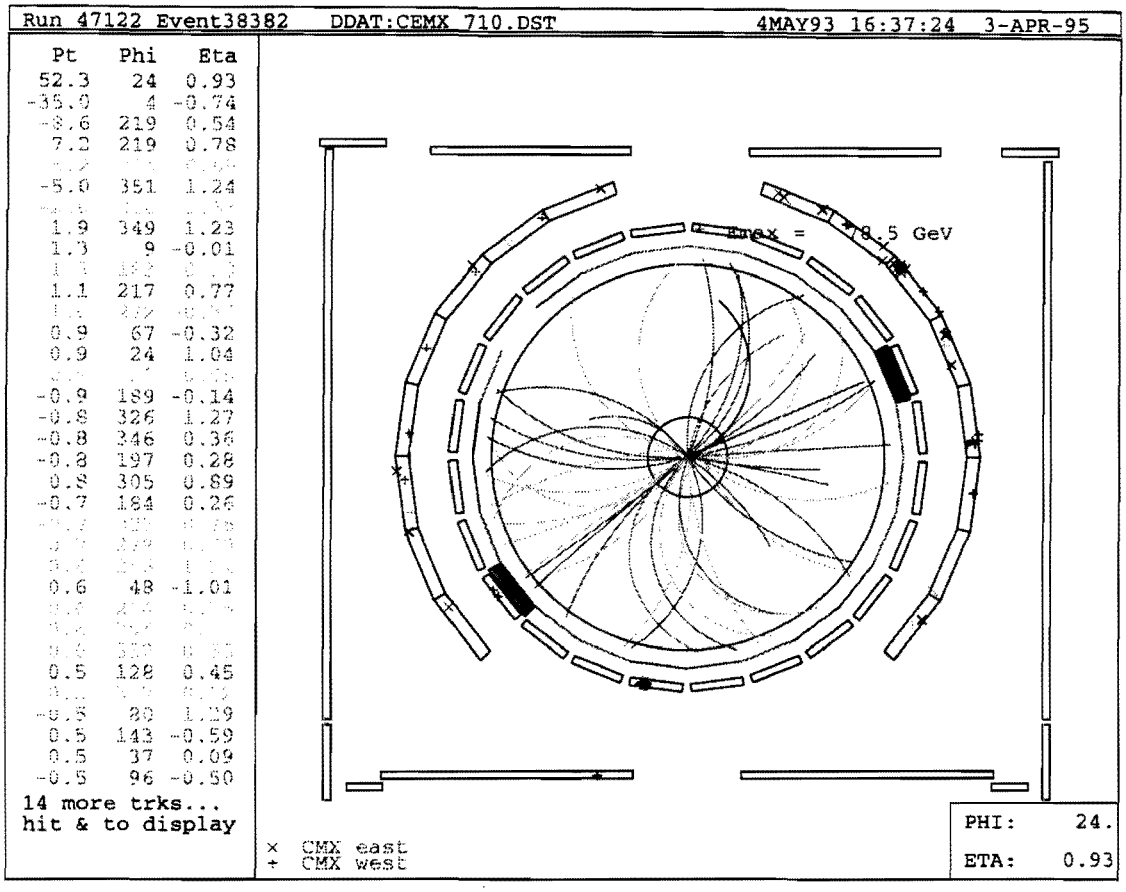

Figure 6.3: The CTC event display for the CEMX event. This is a view looking down the beamline. The muon track is at $\phi = 4°$, and the electron track is at $\phi = 25°$. The central jet is also visible at $\phi = 85°$. The central calorimeter energy depositions are shown, with the darker shading indicating the electromagnetic energy, and the lighter shading indicating the hadronic energy. Further out in radius are the hits in the CMU, CMX, and CMP chambers.

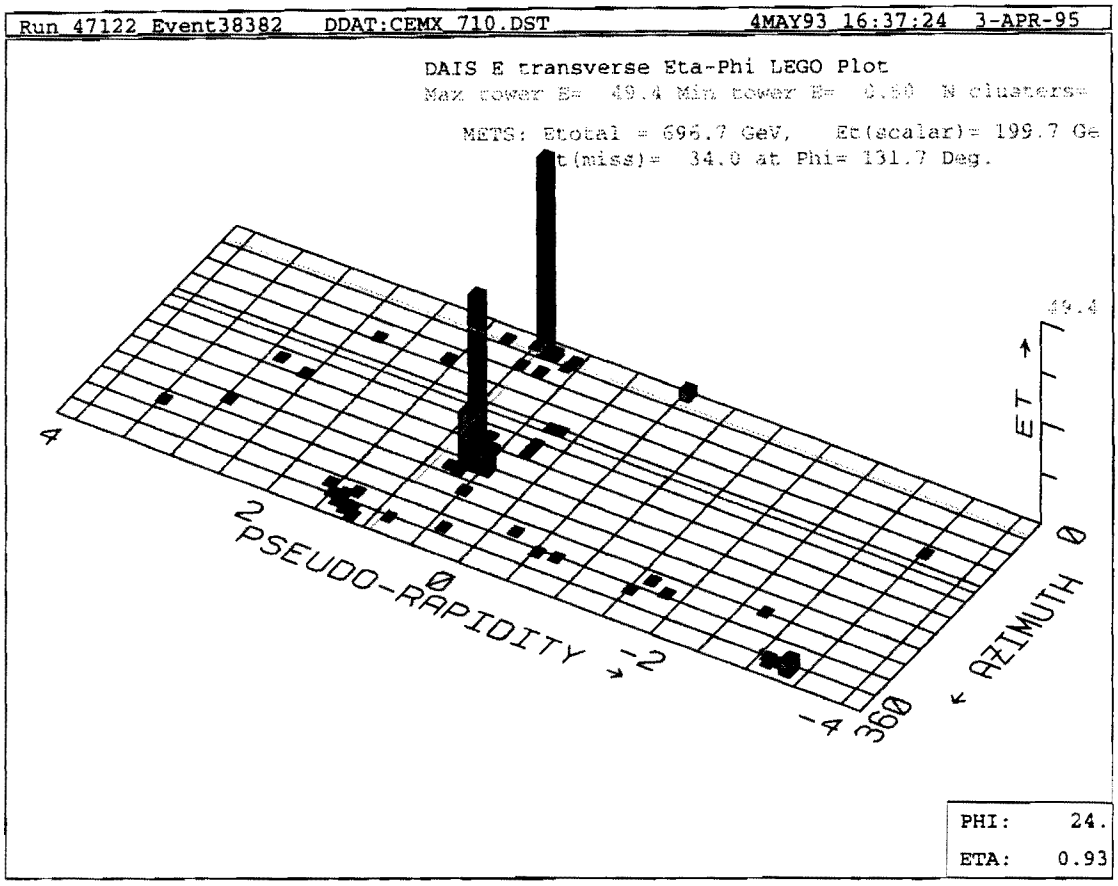

Figure 6.4: The calorimeter event display for the CEMX event. The darker shading represents energy in the electromagnetic calorimeters, and the lighter shading represents energy in the hadronic calorimeters.

to 2 or more events is 6.2%. Thus, we cannot rule out with certainty that

Object	p_T (GeV/c) before jet corrections	p_T (GeV/c) after jet corrections	η	ϕ
e^+		50.6	0.93	25°
μ^-		37.3	−0.74	4°
Jet 1	67.0	85	0.64	218°
Jet 2	10.7	26	1.34	344°
Jet 3	13.6	18	−3.31	344°
$\not\!\!E_T$		60		149°

Table 6.2: Properties of the CEMX event. The energy corrections for Jet 1 and Jet 2 have been done assuming that they are b quark jets. The energy correction for Jet 3 has been done assuming that it is a light quark or gluon jet.

the 2 observed events are caused by an upward fluctuation of the background. Nevertheless, the most natural explanation for the observed excess of events over the expected background is to attribute them to $t\bar{t}$ pair production. The observed secondary vertex in the DPF event adds credibility to this hypothesis, as does the fact that no additional are seen when the two-jet, $\not\!\!E_T$ direction, and opposite sign of electric charge cuts are relaxed. More recent results from the CDF [11] and D0 [12] collaborations confirm the existence of the top quark, with masses of $176 \pm 8 \pm 10$ GeV/c^2 and $199^{+19}_{-21} \pm 22$ GeV/c^2, respectively. We conclude that this analysis has provided some of the earliest evidence for $t\bar{t}$ pair production.

We can extract a cross-section for the process $\bar{p}p \rightarrow t\bar{t}$ at $\sqrt{s} = 1.8$ TeV. Since the total detection efficiency for $t\bar{t}$ events depends on the value of m_{top}, so does the cross-section we calculate. We perform a background subtraction, divide by the total detection efficiencies listed in Table 4.20 and divide by an integrated luminosity of 19.3 ± 0.7 pb^{-1} to find the $t\bar{t}$ production

m_{top}(GeV/c^2)	$\sigma_{t\bar{t}}$ (pb)
100	$31.7\ ^{+50.9}_{-24.9} \pm 12.4$
120	$18.6\ ^{+29.8}_{-14.7} \pm 3.0$
140	$14.0\ ^{+22.5}_{-11.1} \pm 1.7$
160	$12.6\ ^{+20.2}_{-9.9} \pm 1.4$
180	$11.2\ ^{+18.1}_{-8.9} \pm 1.2$
200	$11.2\ ^{+18.1}_{-8.9} \pm 1.2$

Table 6.3: The measured $t\bar{t}$ production cross-section for several values of m_{top}. The first set of uncertainties includes the uncertainty in the number of expected background events and is calculated using from the Poisson formula. The second set of uncertainties includes the uncertainty in the efficiency as well as the uncertainty in the integrated luminosity.

cross-section for several values of m_{top}. These cross-sections are shown in Table 6.3. The first set of uncertainties in this table take into account the Poisson distribution of the number of expected events as well as the uncertainty in the background estimation. The second set of uncertainties includes the uncertainty in the total detection efficiency and the 3.6% uncertainty in the integrated luminosity [10].

The theoretical $t\bar{t}$ production cross-section depends strongly on the mass of the top quark. A next-to-leading-order calculation [48] predicts the production cross-section at the Tevatron to be approximately 100 pb for $m_{top} \approx 100$ GeV/c^2, with the cross-section falling smoothly as m_{top} increases. For $m_{top} \approx 200$ GeV/c^2, the predicted cross-section is approximately 2 pb. Figure 6.5 shows the theoretical $t\bar{t}$ production cross-section [48] overlaid with the cross-section measurement provided by this analysis. Because of the large statistical uncertainty, the cross-section we measure is consistent with all values of the top quark mass within the range 100 GeV/c^2 $< m_{top} <$ 200 GeV/c^2.

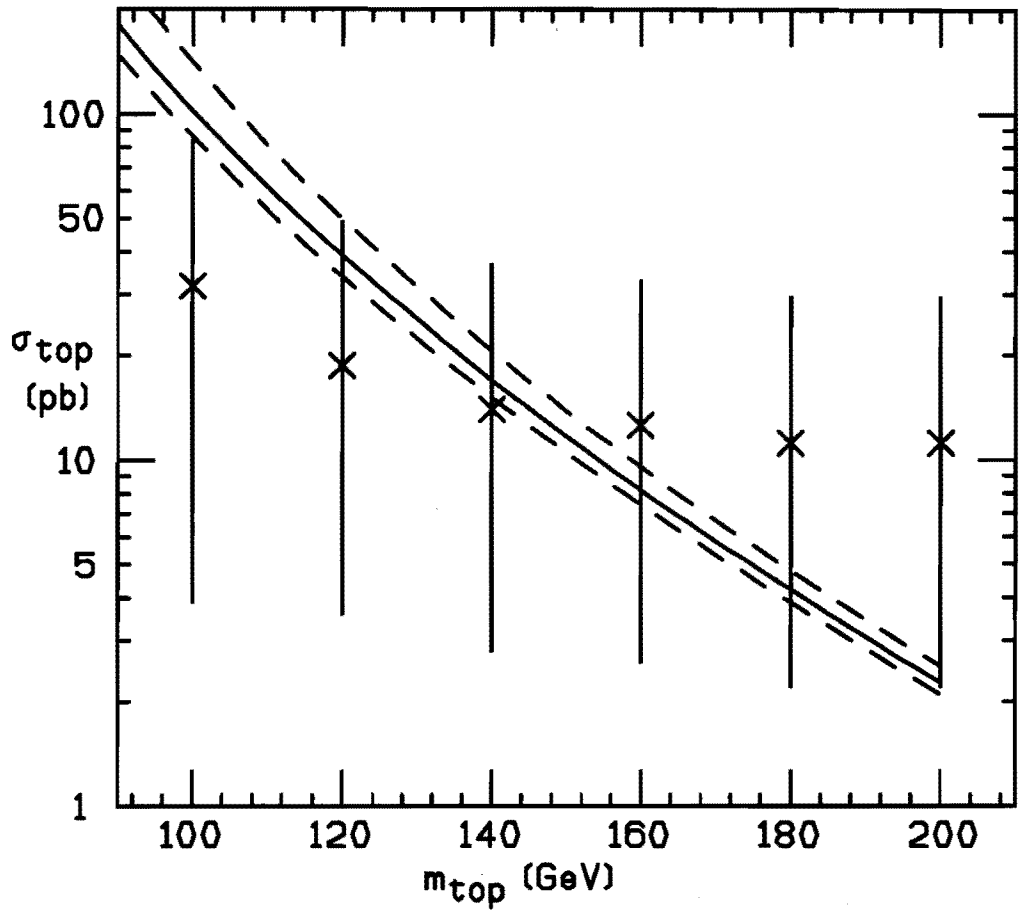

Figure 6.5: Comparison of the theoretical $t\bar{t}$ production cross-section and the $t\bar{t}$ production cross-section measured in this analysis. The solid and dashed curves are the central value and the 1σ bounds of the theoretical $t\bar{t}$ cross-section from Reference [48]. The crosses indicate the $t\bar{t}$ production cross-section measurement provided by this analysis, shown for several values of m_{top}.

Appendix A

OTHER INTERESTING DILEPTON EVENTS

The data contain two events satisfying the selection criteria of this analysis. These two events are described in Chapter 6. There are in addition several events with two leptons which lie near, but not in, the signal region of this analysis, and which may be of interest because they contain jets with identified secondary vertices [49]. This appendix will catalogue some of the characteristics of four of these events.

A.1 Event 38366 of Run 42446

This event contains a $\mu^+\mu^-$ pair and 3 jets. Table A.1 lists some of the characteristics of the objects in this event. The μ^- track is matched to hits in both the CMU and CMP muon chambers, and the μ^+ track is matched to CMX muon chamber hits. The muons satisfy the p_T, fiducial, lepton identification and isolation requirements of this analysis. This event fails the Z removal cut, as the invariant mass of the $\mu^+\mu^-$ pair is 92.6 GeV/c^2. This event also fails

the $\not\!\!E_T$ cuts, as can be seen in Table A.1. The JETVTX algorithm finds a secondary vertex in Jet 1 of that table. This secondary vertex is a distance of 0.908 ± 0.069 cm from the beamline. Jet 2 and Jet 3 are very close to each other. When the jet clustering algorithm is run using a cone size of $R = 0.7$, these two jets are reconstructed as a single jet.

Object	p_T (GeV/c) before jet corrections	p_T (GeV/c) generic jet corrections	p_T (GeV/c) b jet corrections	η	ϕ
μ^-	20.8			-0.36	300.0°
μ^+	67.7			$+0.98$	123.7°
Jet 1	37.5	60.9	60.7	$+1.13$	192.2°
Jet 2	21.3	32.7	38.6	-0.75	348.3°
Jet 3	21.4	32.0	38.0	-0.54	316.4°
$\not\!\!E_T$		34.4			359.2°

Table A.1: Properties of event number 38366 of run 42446. $\not\!\!E_T$ has been computed using the generic (light quark or gluon) jet corrections for all jets.

A.2 Event 198920 of Run 43170

This is the single event which satisfies all of the requirements of this analysis except for the Z removal cut, and which figures heavily in the estimation of the background due to Drell-Yan production of lepton pairs, described in Chapter 5. This event contains a $\mu^+\mu^-$ pair and 2 jets. Table A.2 lists some of the characteristics of the objects in this event. Both muon tracks are matched to hits in both the CMU and CMP muon chambers. The invariant mass of the $\mu^+\mu^-$ pair is 101.7 GeV/c^2. Figure 4.3 shows the mass distributions of ee and $\mu\mu$ events. Recall that the Z removal cut rejects ee and $\mu\mu$ events where the invariant mass of the two leptons is between 75 and

105 GeV/c^2. The JETVTX algorithm finds a secondary vertex in Jet 1 in Table A.2. The secondary vertex is a distance of 0.402 ± 0.007 cm from the beamline.

Object	p_T (GeV/c) before jet corrections	p_T (GeV/c) generic jet corrections	p_T (GeV/c) b jet corrections	η	ϕ
μ^-	71.6			+0.16	17.0°
μ^+	37.2			+0.38	220.3°
Jet 1	78.9	103.6	97.3	+0.37	119.3°
Jet 2	64.3	85.6	81.4	+0.19	238.0°
$\not\!\!E_T$		58.7			344.0°

Table A.2: Properties of event number 198920 of run 43170. $\not\!\!E_T$ has been computed using the generic (light quark or gluon) jet corrections for all jets.

A.3 Event 104393 of Run 45047

This event contains an electron candidate, a muon, and 2 jets. Table A.3 lists some of the characteristics of the objects in this event. The muon track is matched to hits in both the CMU and CMP muon chambers. The electron candidate satisfies the loose set of electron identification requirements, but does not satisfy the tight set of electron identification requirements. These requirements are listed in Table 4.4. Specifically, the electron fails the E^{had}/E^{em} and χ^2_{strip} requirements. This electron candidate has values of $E^{had}/E^{em} = 6.0\%$ and $\chi^2_{strip} = 20.7$ for these quantities, while the cuts are set at 5.0% and 15.0, respectively. Figure 3.3 shows the distributions of these variables for electrons in Z events. It can be seen that the E^{had}/E^{em} and χ^2_{strip} values for the electron candidate in this event are far into the tails

of the distributions. This event satisfies all of the other selection criteria of this analysis. The JETVTX algorithm finds a secondary vertex in Jet 1 of Table A.3. The secondary vertex is a distance of 0.669 ± 0.019 cm from the beamline. The track of the electron candidate also has a large impact parameter. The electron candidate leaves hits in each of the four SVX layers, and has an impact parameter of 0.041 ± 0.002 cm from the beamline. This invites the interpretation of this object as an electron from the decay $\tau \rightarrow e\nu\nu$. Of course this is merely speculation, as it is far from certain whether this candidate is an electron at all.

Object	p_T (GeV/c) before jet corrections	p_T (GeV/c) generic jet corrections	p_T (GeV/c) b jet corrections	η	ϕ
μ^-	39.1			-0.36	116.6°
e^+	23.6			$+0.43$	252.6°
Jet 1	44.0	72.0	69.8	-1.20	117.7°
Jet 2	22.5	34.2	39.8	$+0.91$	117.7°
$\not\!\!E_T$		129.1			310.5°

Table A.3: Properties of event number 104393 of run 45047. $\not\!\!E_T$ has been computed using the generic (light quark or gluon) jet corrections for all jets.

A.4 Event 314567 of Run 46870

This event contains an e^+e^- pair and 4 jets. Table A.4 lists some of the characteristics of the objects in this event. The electrons satisfy the p_T, fiducial, lepton identification and isolation requirements of this analysis. This event fails the Z removal cut, as the invariant mass of the e^+e^- pair is 92.2 GeV/c^2. This event also fails the $\not\!\!E_T$ cuts, as can be seen in Table A.4.

The JETVTX algorithm finds a secondary vertex in Jet 1 of that table. This secondary vertex is a distance of 0.999 ± 0.029 cm from the beamline.

Object	p_T (GeV/c) before jet corrections	p_T (GeV/c) generic jet corrections	p_T (GeV/c) b jet corrections	η	ϕ
e^-	64.0			+0.45	146.1°
e^+	73.0			−0.41	207.2°
Jet 1	159.2	198.3	184.4	+0.42	352.3°
Jet 2	42.8	55.1	56.0	−1.65	178.4°
Jet 3	34.9	52.9	54.4	+1.32	29.4°
Jet 4	17.0	28.4	35.1	−0.98	166.3°
$\not\!\!E_T$		37.7			182.3°

Table A.4: Properties of event number 314567 of run 46870. $\not\!\!E_T$ has been computed using the generic (light quark or gluon) jet corrections for all jets.

Appendix B

ACCEPTANCE RELATIVE TO THE DILEPTON BRANCHING RATIO OF 4/81

This analysis focuses on identifying the leptons from the decay of the W bosons in $t\bar{t}$ events. These W decays are not the only source of leptons in $t\bar{t}$ events. The acceptances and efficiencies described in Chapter 4 include contributions from all sources of leptons. In this appendix, we take a closer look at the events where both W bosons decay leptonically (to e or to μ), and look at the acceptance relative to the branching ratio for these events, $4/81 \approx 4.9\%$ (see Table 1.2).

For this study, the ISAJET program was used to generate a $t\bar{t}$ Monte Carlo sample of 100,000 events, with $m_{top} = 175$ GeV/c^2. Table B.1 shows the numbers of these events which have two leptons (e or μ) from W decay,

each with $p_T > 20$ GeV/c, and the numbers of these events where both leptons have $|\eta| < 1$. We see that approximately 42% of the events where both W bosons decay leptonically (e or μ) satisfy these requirements.

The detector response was then simulated with the QFL program. Table B.2 shows the numbers of the Monte Carlo events surviving as successive cuts are applied. It must be noted that the numbers appearing in Table B.2 have not been adjusted for the different lepton identification efficiencies in QFL and data, nor have they been adjusted for trigger efficiency effects. Table B.3 shows the overall efficiencies after correcting for these effects.

Cut	ee	$\mu\mu$	$e\mu$	Total (Relative to $BR = 4/81$)
$p_T > 20$ GeV/c	850	908	1729	70.6%
$p_T > 20$ GeV/c and $\|\eta\| < 1$	497	534	1041	42.0%

Table B.1: The numbers of events in a sample of 100,000 Monte Carlo events generated with $m_{top} = 175$ GeV/c^2, in which two leptons from W boson decay satisfy $p_T > 20$ GeV/c and $|\eta| < 1$ requirements. In this table, p_T and η refer to quantities at the generator level, before the detector response has been simulated. The right-most column gives the acceptance relative to the branching ratio for both W bosons to decay leptonically (e or μ).

Cut	ee	$\mu\mu$	$e\mu$	Total (Relative to $BR = 4/81$)
p_T, fiducial	306	359	887	31.4%
Lepton ID and isolation	203	327	556	22.0%
Z removal	154	237	556	19.2%
$\not\!\!E_T$	125	175	428	14.7%
Two-jet	119	162	392	13.6%
Opposite Sign	119	162	392	13.6%

Table B.2: The numbers of events in a sample of 100,000 Monte Carlo events generated with $m_{top} = 175$ GeV/c^2, in which two leptons from W boson decay satisfy the requirements described in Chapter 4, as the cuts are successively applied. The right-most column gives the acceptance relative to the branching ratio for both W bosons to decay leptonically (e or μ).

Source	ee	$\mu\mu$	$e\mu$	Total (Relative to $BR = 4/81$)
Leptons from W	120.2	135.1	363.7	12.5%
Leptons from all sources	138.5	163.9	441.8	15.1%

Table B.3: The numbers of $t\bar{t}$ events in a Monte Carlo sample of 100,000 events generated with $m_{top} = 175$ GeV/c^2 which satisfy all the selection criteria of this analysis. These numbers have been corrected for trigger efficiency and the difference between QFL and data efficiencies. Numbers are given for events where both leptons come from W boson decay, and for events where all leptons are accepted. The right-most column gives the acceptance relative to the branching ratio for both W bosons to decay leptonically (e or μ).

Appendix C

STUDY OF b QUARK JETS

We expect the final states of the $t\bar{t}$ events we are searching for to contain two b quarks. One of the selection criteria of this analysis is the two-jet cut, which requires events to contain at least two jets, each with $E_T^{raw} > 10$ GeV and $|\eta| < 2.4$. In the future, one may attempt to estimate the top mass from the signal events of this search by employing some type of kinematical reconstruction technique. It is also possible that future studies will require the identification of a displaced secondary vertex in one of the jets. In both of these cases, we would like to know how often the observed jets come from b quarks.

To answer this question, we turn to the Monte Carlo sample described in Appendix B. This sample consists of 100,000 events generated with the ISAJET Monte Carlo program, using a top quark mass of 175 GeV/c^2. After simulating the detector response with the QFL detector simulation program, we find a total of 813 events which pass all the selection criteria of this analysis, including the two-jet cut. Of these 813 events, we find that 804 have at least one b quark jet with $E_T^{raw} > 10$ GeV and $|\eta| < 2.4$, and 656 have two b

quark jets satisfying those requirements. Further, we find that in 474 of the 813 events, the two jets with the largest E_T are b quark jets. Table C.1 summarizes these results. It should be noted that these numbers depend fairly strongly on the value of m_{top}, as does the efficiency of the two-jet cut. We have chosen $m_{top} = 175$ GeV/c^2 for this study because it is near the value of 174 ± 17 GeV/c^2 reported by the CDF collaboration [11].

Probability of observing at least one b jet	98.9%
Probability of observing two b jets	80.7%
Probability that the two leading observed jets are both b jets	58.3%

Table C.1: Probabilities of observing b quark jets. These numbers are relative to the number of events which satisfy all the selection criteria of this analysis, including the two-jet requirement. These numbers are found from a Monte Carlo sample which was generated with $m_{top} = 175$ GeV/c^2. Only jets with ${E_T}^{raw} > 10$ GeV and $|\eta| < 2.4$ are considered in this study.

REFERENCES

[1] S. Glashow, Nucl. Phys. **22**, 579 (1961); S. Weinberg, Phys. Rev. Lett. **19**, 1264 (1967); A. Salam, in *Elementary Particle Theory: Relativistic Groups and Analyticity (Nobel Symposium No. 8)*, edited by N. Svartholm (Almqvist and Wiksell, Stockholm, 1968), p. 367.

[2] S. Glashow, J. Illiopoulos, and L. Maiani, Phys. Rev. D **2**, 1285 (1970); M. Kobayashi and M. Maskawa, Prog. Theor. Phys. **49**, 652 (1973); N. Cabibbo, Phys. Rev. Lett. **10**, 531 (1963).

[3] For a general review of gauge theories, the Standard Model, and triangle anomalies, there are many excellent texts. I reference three of these here, but this is by no means an exhaustive list. F. Halzen and A. Martin, *Quarks and Leptons: An Introductory Course in Modern Particle Physics*, John Wiley & Sons, New York, 1984; C. Quigg, *Gauge Theories of the Strong, Weak, and Electromagnetic Interactions*, Addison-Wesley Publishing Company, New York, 1983; L. Ryder, *Quantum Field Theory*, Cambridge University Press, Cambridge, 1985.

[4] P. Higgs, Phys. Rev. Lett. **12**, 132 (1964).

[5] S. Herb *et al.*, Phys. Rev. Lett. **39**, 252 (1977); W. Innes *et al.*, Phys. Rev. Lett. **39**, 1240 (1977).

[6] If the b were an iso-singlet, the decay $B \rightarrow l^+l^-X$ should occur at a rate far greater than the observed rate, see A. Bean *et al.*, Phys. Rev. D **35**, 3533 (1987). Measurement of the forward-backward asymmetry and the the partial width $\Gamma(Z \rightarrow b\bar{b})$ at LEP identify the b quark as the lower component of the left-handed iso-doublet, see, for example, P. Wells, CERN-PPE/94-203, "Heavy Quark Physics at LEP," a talk presented at the XXII Summer Institute on Particle Physics, August, 1994.

[7] J. Steinberger, Phys. Rev. **76**, 1180 (1949); J. Schwinger, Phys. Rev. **82**, 664 (1951); D. Sutherland, Phys. Lett. **23**, 384 (1966); D. Sutherland, Nucl. Phys. **B2**, 433 (1967); S. Adler, Phys. Rev. **177**, 2426 (1969); J. Bell and R. Jackiw, Nouvo Cimento, **60A**, 47 (1967).

[8] F. Abe *et al.*, Phys. Rev. D **45**, 3921 (1992).

[9] S. Abachi *et al.*, Phys. Rev. Lett. **68**, 447 (1994).

[10] F. Abe *et al.*, Phys. Rev. D **50**, 2966 (1994); F. Abe *et al.*, Phys. Rev. Lett. **73**. 225 (1994).

[11] F. Abe *et al.*, Phys. Rev. Lett. **74**, 2626 (1995).

[12] S. Abachi *et al.*, Phys. Rev. Lett. **74**, 2632 (1995).

[13] F. Abe *et al.*, Nuc. Inst. Methods Phys. Res. A, **271**, 387 (1988). In addition to this published work, excellent and somewhat less technical descriptions may be found in the following theses: S. Kopp, Ph. D. dissertation, University of Chicago, 1994; P. Derwent, Ph. D. dissertation, University of Chicago, 1990; and M. Contreras, Ph. D. dissertation, Brandeis University, 1990.

[14] F. Abe *et al.*, Fermilab Report No. Fermilab-Pub-94/024-E, 1994 (unpublished).

[15] CDF internal note #1172, "Proposal for an Upgraded CDF Detector."

[16] F. Bedeschi *et al.*, Nuc. Inst. Methods Phys. Res. A, **228**, 50 (1988).

[17] L. Balka *et al.*, Nuc. Inst. Methods Phys. Res. A, **267**, 272 (1988).

[18] S. Bertolucci *et al.*, Nuc. Inst. Methods Phys. Res. A, **267**, 301 (1988).

[19] Y. Fukui *et al.*, Nuc. Inst. Methods Phys. Res. A, **267**, 280 (1988).

[20] M. Franklin *et al.*, Proceedings of the VII Topical Workshop on Proton-Antiproton Collider Physics, p. 420, published by World Scientific (1988).

[21] G. Brandenburg *et al.*, Nuc. Inst. Methods Phys. Res. A, **267**, 257 (1988).

[22] S. Cihangir *et al.*, Nuc. Inst. Methods Phys. Res. A, **267**, 249 (1988).

[23] G. Ascoli *et al.*, Nuc. Inst. Methods Phys. Res. A, **268**, 33 (1988).

[24] CDF internal note #1500, "Design and Performance of Drift Chambers for the Central Muon Upgrade."

[25] CDF internal note #1614, "Study of the Performance of the CMEX Drift Tubes."

[26] CDF internal note #250, "Beam-beam Counters for CDF."

[27] D. Amidei *et al.*, Nuc. Inst. Methods Phys. Res. A, **269**, 51 (1988); G. Ascoli *et al.*, Nuc. Inst. Methods Phys. Res. A, **269**, 63 (1988); G. Foster *et al.*, Nuc. Inst. Methods Phys. Res. A, **269**, 93 (1988).

[28] U. Joshi *et al.*, Nuc. Phys. B, **23A**, 363 (1991).

[29] G. Foster *et al.*, Nuc. Inst. Methods Phys. Res. A, **269**, 93 (1988).

[30] F. Abe *et al.*, "A Measurement of the Ratio $\sigma \cdot B(p\bar{p} \rightarrow W \rightarrow e\nu)/\sigma \cdot B(p\bar{p} \rightarrow Z^0 \rightarrow ee)$ in $p\bar{p}$ Collisions at $\sqrt{s} = 1800/GeV$," submitted to Phys. Rev. D. (1994); S. Kopp, Ph. D. dissertation, University of Chicago, 1994.

[31] CDF internal note #2217, "Measurement of R(μ) in Proton-Antiproton Collisions."

[32] F. Abe *et al.*, Phys. Rev. D **45**, 1448 (1992); F. Abe *et al.*, Phys. Rev. D **47**, 4857 (1993).

[33] CDF internal note #1810, "A User's Guide to QFL," and CDF internal note #2177, "CDFSIM + QFL Simulation of the CDF Detector."

[34] J. Ohnemus *et al.*, Phys. Rev. D **44**, 1403 (1991); S. Frixone, Nucl. Phys. **B410**, 280 (1993).

[35] P. Avery, K. Read, and G. Trahern, Cornell Internal Note CSN-212 1985 (unpublished).

[36] Particle Data Group, L. Montanet *et al.*, Phys. Rev. D **50**, 1405 (1994).

[37] F. Abe *et al.*, Phys. Rev. D **44**,29 (1991).

[38] J. Gunion and Z. Kunszt, Phys. Lett. **161B**, 333 (1985); R. Kleiss and W. Stirling, Nucl. Phys. **B262**, 235 (1985); K. Hagiwara and D. Zeppenfeld, Nucl. Phys. **B313**, 560 (1989); F. Berends, W. Giele, and H. Kuijf, Nucl. Phys. **B321**, 39 (1989); F. Berends *et al.*, Nucl. Phys. **B357**, 32 (1991). Michelangelo Mangano performed the calculations of these corrections for this analysis.

[39] F. Paige and S. D. Protopopescu, BNL Report No. 38034, 1986 (unpublished).

[40] We use two sets of criteria for identifying electrons from photon conversions. The first method looks for the observed number of hits in the Vertex Tracking Chamber (VTX) to be less than 20% of the number of hits expected for a prompt electron. The second method searches for a charged particle tracks in the Central Tracking Chamber (CTC) which have the opposite sign of electric charge as the electron track, and where the invariant mass of the two tracks is less than 0.5 GeV/c^2. If either set of criteria is satisfied, the electron is considered to be a conversion electron and is excluded from the analysis presented in this thesis.

[41] The uncertainties in these quantities are asymmetric. The uncertainties have been caculated according to the binomial distribution. For typographical reasons, the larger of the upper and lower uncertainties found from this calculation is chosen and displayed in the table.

[42] F. Abe *et al.*, Phys. Rev. D **43**, 2070 (1991).

[43] Jinsong Wang and Linfeng Song each spent many months generating the $b\bar{b}$ Monte Carlo samples used in the study of this background.

[44] The cuts have been tightened in order to guarantee that the 18 GeV/c lepton satisfies the trigger and offline identification requirements necessary for the event to make it into inclusive single lepton samples. These inclusive lepton samples were stripped from the 194 tapes of express stream data, just as the dilepton sample was.

[45] The calculation of the $\tau\tau$ background was done using the τ simulation routines provided by Jinsong Wang. I reference his thesis here. Jinsong Wang, Ph. D. dissertation, University of Chicago, 1994.

[46] S. Drell and T. Yan, Phys. Rev. Lett. **25**, 316 (1970).

[47] The distribution is shown for Monte Carlo events generated with a top quark mass of 160 GeV/c^2. Recent results from the CDF[11] and D0[12] collaborations confirm the existence of the the top quark at masses of $176 \pm 8 \pm 10$ GeV/c^2 and $199^{+19}_{-21} \pm 22$ GeV/c^2, respectively. The analysis presented in this thesis was carried out before these results from the CDF and D0 collaborations were available. We have chosen the distribution from the $m_{top} = 160$ GeV/c^2 Monte Carlo as illustrative of a typical distribution. The distribution is not particularly senstive to the value of m_{top}.

[48] E. Laenen *et al.*, Phys. Lett. B **321**, 254 (1994).

[49] The secondary vertex information was provided by Weiming Yao, who ran the JETVTX algorithm on these events.

[50] CDF internal note #1975, "Top Dilepton Analysis." This document contains a detailed description of the dilepton analysis and represents the work of many people, among whom are T. Chikamatsu, A. Martin, J. Wang, A. Beretvas, M. Contreras, L. Demortier, H. Frisch, S. Kopp, Y. Seiya, L. Song, L. Stanco, C. Wendt, Q. F. Wang, and G. P. Yeh. In this thesis, I summarize the results of the systematics study performed by T. Chikamatsu, and described in the CDF internal note.